

# Evolving Gaussian Processes for Learning and Control in Spatiotemporally Varying Domains

with applications in agriculture, weather monitoring, and fluid dynamics

Harshal Maske, Hassan Kingravi, Joshua Whitman, Girish Chowdhary,  
POC email: girishc@illinois.edu

## Introduction

Monitoring and modeling of large-scale stochastic phenomena with both spatial and temporal (spatiotemporal) evolution using a network of distributed sensors is a fundamental problem in the applied sciences. Consider, for example, a team of mechanical weeding robots managing herbicide-resistant weeds on a farm (see Figure 1, also see the sidebar on control problems in agriculture). This team of robots needs to predict the weed growth across the whole farm in real time to make intelligent decisions on robot coordination [1]. However, the robots can only observe a limited part of the field at any given time. With rapid advances in robotics and the capability to process large volumes of data on compact computational packages, the applications for such distributed Cyber Physical Systems are rapidly expanding. Common examples include modeling and monitoring ocean heat content and acidification in oceanography using a network of satellites and surface sensors; prediction of traffic patterns using data from vehicles, cellphones, and traffic cameras; prediction of enemy movements through ground and aerial surveillance, and prediction of spatiotemporal evolution of extreme weather events using data from weather stations and aerial drones.

These types of problems are characterized by complex and stochastic dynamics that are distributed in space and time. While modeling such spatiotemporal phenomena has traditionally been the province of the field of geostatistics, it has in recent years gained more attention in the machine learning community [2]. The data-driven models developed through machine learning techniques provide a way to capture complex spatiotemporal phenomena which are not easily modeled by first-principles alone. However, machine learning models are limited by the data sets they are trained on, and the challenge with complex and distributed physical systems is that they have very high amounts of variability. For example, a model trained on weed growth over years of data in one field doesn't necessarily generalize to another, and a model trained on past

few year's worth of data is still unreliable to predict weather variability in the following year. What is needed instead of just a *predict* system is a *predict-and-correct* system; we elucidate this point below in more detail.

In the machine learning community, kernel methods represent a class of extremely well-studied and powerful methods for regression in spatial domains. In these techniques, correlations between the input variables are encoded through covariance kernels, and the model is formed through a linear weighted combination of the kernels [3]–[5]. In recent years, kernel methods have been applied to spatiotemporal regression problems with varying degrees of success [2], [3]. Many recent techniques in spatiotemporal modeling have focused on nonstationary covariance kernel design and associated hyperparameter learning algorithms [6]–[8]. These methods, which focus on the careful design of covariance kernels, have been proposed as an alternative to the naive approach of simply including time as an additional input variable in the kernel [9]. The careful design/optimization of covariance kernel avoids an explosion in the number of parameters (kernels utilized) of the model which would be inevitable in a model that simply adds time as an additional input variable, and has been shown to better account for spatiotemporal couplings.

However, there are two key challenges with existing kernel-based and (for that matter) other machine learning approaches for prediction over complex spatiotemporally-varying physical systems: The first is ensuring the scalability of the model to large scale phenomena, which manifests due to the fact that the problem of optimizing the covariance kernel (known as hyperparameter optimization in the ML community) is not convex in general, leading to methods that are difficult to implement especially in online settings, susceptible to getting stuck at local minima, and highly computationally demanding for large datasets [10]. This has also been a key issue in utilizing deep learning models for this problem. The second key challenge is that no matter how much data the model is trained on, it cannot completely capture the variability in real world complex systems with spatiotemporal dynamics. This is a problem that the controls community is quite aware of. Our solutions to this problem build upon feedback, leading to fundamental notions of observability and controllability which can be used to build robust state estimators and controllers. To bring these notions to fruition in the spatiotemporal prediction problem, what is needed is a way to inform where sensing/control should be done to ensure that the state estimation problem can be made observable/controllable. It is however not clear how notions of observability and controllability could be utilized with existing kernel-based machine learning models, and how observers and controllers can be embedded within such models. While the computational challenge can be addressed with increasing computational power and large datasets, addressing the latter (and vastly more fundamental) challenge in designing robust observers/controllers is particularly important in the design of reliable engineering systems, such as distributed sensor/actuator networks intended for monitoring physical phenomena, autonomous

soft-robots, or other physical systems with distributed sensing and actuation.

## Contributions

In this article, we present a new perspective on solving the spatiotemporal monitoring problem that brings together kernel-based modeling, systems theory, and Bayesian filtering.

5 We define the monitoring problem as follows: *Given an approximate predictive model of the spatiotemporal phenomena learned using historic data, estimate the current latent state of the phenomena in the presence of uncertainty using as few sensors as possible.* Ideally, the solution to the problem should also provide guidance on how many sensors are needed and where to place them. In this paper we argue that when it comes to predictive inference over spatiotemporal

10 phenomena, a Kalman-filter type approach of predicting and correcting with feedback from a set of minimal sensors is a robust way of dealing with real-world uncertainties and inherent modeling errors. In the context of this specific problem, *our main contributions are two-fold:* first, we demonstrate that spatiotemporal functional evolution can be modeled using stationary kernels with a linear dynamical systems layer on their mixing weights. In particular, in contrast with

15 existing work, this approach does not necessarily require the design of complex spatiotemporal kernels, and can accommodate positive-definite kernels on any domain on which it is possible to define them, which includes non-Euclidean domains such as Riemannian manifolds, strings, graphs and images [11]. Second, we show that such a model can be utilized to determine sensing locations that guarantee that the hidden states of functional evolution can be estimated using a

20 Bayesian state-estimator (Kalman filter) that is *embedded in the feature space of the kernel model* with very few sensors. A benefit of our solution approach is that it provide guidance on how many sensors are needed and where to place them. Accordingly, we provide sufficient conditions on the number and location of sensor measurements required and prove non-conservative lower bounds on the minimum number of sampling locations by developing fundamental results on the

25 observability of kernel-based models. The validity of the presented model and sensing techniques is corroborated using synthetic and large real datasets.

### Broader Context

The fundamental idea of building observers and controllers embedded in the feature spaces of machine learning models introduced in this paper is generalizable beyond the particular

30 application of spatiotemporal monitoring. Indeed, the contributions of this paper demonstrate how machine learning machine learning theory can be fused with systems theory to address major challenges in distributed monitoring and control of complex spatiotemporally varying systems. We elucidate this point below.

Traditionally, the controls literature is strongest when the system dynamics can be

represented as ODEs. As depicted in Figure 2, some of the major successes of controls have included results such as LQG, reinforcement learning, and adaptive control in state spaces with well-defined, finite, and physically meaningful state variables. The problem of state estimation of a temporally evolving, finite-dimensional state-space system for example has been  
5 extensively studied in the context of Kalman filtering and observer design [12]. Here, fundamental results in observability/controllability provide sufficient conditions on the structure of the state transition and measurement matrix such that the latent state can be estimated in the presence of measurement and process noise. On the other hand, machine learning models operate in an abstract and learned function-space of *features* (see sidebar *Feature Spaces in Machine Learning*).  
10 Kalman filters can be naively extended to the functional domain (e.g. [13]), but have not typically been studied in context of the spatiotemporal monitoring problem studied here.

On the other hand, recent advances in machine learning are providing different and highly powerful ways of modeling complex spatiotemporal dynamical systems. Yet, the main challenge with using machine learning approaches such as deep learning or kernel based methods has  
15 been that these approaches lack interpretability and analyzability, which makes it difficult to design robust engineered systems. This is mostly because machine learning works in abstract feature spaces that are only relatable to physical quantities through complex functional operations (see sidebar *Feature Spaces in Machine Learning* for discussion on feature spaces in machine learning). This leads to a major challenge in using machine learning models in control: For  
20 example, when kernel based models are used for spatiotemporal systems, how does one answer fundamental questions such as 1) the least number of sensors required to observe a distributed system, 2) the placement of sensors/actuators to guarantee observability/controllability of the system, and 3) the effect of random sensor placement on system observability/controllability.

In this paper we present an approach that can provide one formal way of addressing these  
25 and other questions about complex systems that are modeled with machine learning. In particular, we demonstrate how linear dynamical systems can be embedded in the reproducing kernel Hilbert space (RKHS) [4], [14], [15] generated by features used in Gaussian Process modeling [16], [17], and utilized to answer fundamental questions such as controllability and observability. The marriage of systems theory with machine learning pursued in this paper is exciting, and we  
30 expect that follow-up work will exploit the framework presented in this paper of utilizing linear models in RKHSs and feature spaces of other machine learning models to enable practical and analyzable data-driven engineering systems. To facilitate the development of the theory, we have focused this paper on the problem of monitoring spatiotemporal phenomena. However, the idea should be generalizable to any distributed cyber-physical system that is changing with space and  
35 time.

We begin the rest of the article by summarizing some related work in machine learning in this area. Sidebar *Feature Spaces in Machine Learning* outlines feature spaces in machine learning in a broader context. We then formulate the problem, introduce *Kernel Observers (KO)*, and develop the main theoretical and algorithmic results. This is followed by some results on the 5 expected number of randomly placed sensors required to monitor a spatiotemporal process in the context of our model. An extension to the KO method called *Evolving Gaussian Processes (E-GP)* is presented that learns one model for multiple, similar spatiotemporal processes, the efficacy of which on real-world CFD data is presented in Sidebar *Learning Fluid Flows with Evolving Gaussian Processes*, which concludes the paper. Elements of the work presented 10 in this paper first appeared in the premier machine learning conference Neural Information Processing Systems (NIPS 2016) ([18], [19]), IEEE CDC 2015 conference [20], the Conference on Robot Learning (CoRL 2017) [21] and IEEE ACC 2018 conference [22]. This paper presents a comprehensive set of results and fills in the missing links in a single encompassing publication, and introduces new results on observability in the presence of random sensor placement. As such, 15 we have focused in this article mostly on the fundamental theory and practical algorithms for modeling, estimation, and control, while the excruciating details of how to optimally implement the presented algorithms are omitted<sup>1</sup>.

## Related Work

There is a large body of literature on spatiotemporal modeling in geostatistics where specific 20 process-dependent kernels can be used [2], [23]. From the machine learning perspective, a naive approach is to utilize both spatial and temporal variables as inputs to a Mercer kernel [24]. However, this technique leads to an ever-growing kernel dictionary. Furthermore, constraining the dictionary size or utilizing a moving window will occlude learning of long-term patterns. Periodic or nonstationary covariance functions and nonlinear transformations have been proposed 25 to address this issue [3], [7]. Work focusing on nonseparable and nonstationary covariance kernels seeks to design kernels optimized for environment-specific dynamics, and to tune their hyperparameters in local regions of the input space. Seminal work in [25] proposes a process convolution approach for space-time modeling. This model captures nonstationary structure by allowing the convolution kernel to vary across the input space. This approach can be extended 30 to a class of nonstationary covariance functions, thereby allowing the use of a Gaussian process (GP) framework, as shown in [26]. However, since this model's hyperparameters are inferred using MCMC integration, its application has been limited to smaller datasets. To overcome

<sup>1</sup>Instead an open-source code-base is made available in MATLAB at <http://daslab.illinois.edu/software.html> or at <https://github.com/hkingravi/FunctionObservers> and in Python on GitHub at <https://github.com/hkingravi/funcobspy>.

this limitation, [8] proposes to use the mean estimates of a second isotropic GP (defined over latent length scales) to parameterize the nonstationary covariances. Finally, [6] considers non-isotropic variation across different dimension of input space for the second GP as opposed to isotropic variation by [8]. Issues with this line of approach include the nonconvexity of the 5 hyperparameter optimization problem and the fact that selection of an appropriate nonstationary covariance function for the task at hand is a nontrivial design decision (as noted in [27]).

Apart from directly modeling the covariance function using additional latent GPs, there exist several other approaches for specifying nonstationary GP models. One approach maps the nonstationary spatial process into a latent space, in which the problem becomes approximately 10 stationary [28]. Along similar lines, [29] extends the input space by adding latent variables, which allows the model to capture nonstationarity in original space. Both these approaches require MCMC sampling for inference, and as such are subject to the limitations mentioned in the preceding paragraph.

A geostatistics approach that finds dynamical transition models on the linear combination 15 of weights of a parameterized model [2], [13] is advantageous when the spatial and temporal dynamics are hierarchically separated, leading to a convex learning problem. As a result complex nonstationary kernels are often not necessary (although they can be accommodated). The approach presented in this paper aligns closely with this vein of work. A systems-theoretic study of this viewpoint enables the fundamental contributions of the paper, which are 1) 20 allowing for inference on more general domains with a larger class of basis functions than those typically considered in the geostatistics community, and 2) quantifying the minimum number of measurements required to estimate the state of the system.

Lastly, sensor placement optimization is also a well-studied area. Examples include, but 25 are not limited to 1) geometric approaches, which seek to provide a covering of the operating space without making assumptions about the spatiotemporal dynamics [30], and 2) information-theoretic approaches, which place their focus on sensor placement optimizing strategies based on mutual information and information entropy for Gaussian process models [31]. It should be noted that the contribution of the paper concerning sensor placement is to provide *sufficient conditions* for monitoring rather than optimization of the placement locations, and therefore a 30 comparison with these approaches is not considered in the experiments.

## Kernel Observers

This section outlines our modeling framework and presents theoretical results associated with the number of sampling locations required for monitoring functional evolution.

## Problem Formulation

We focus on predictive inference of a time-varying stochastic process, whose mean  $f$  evolves temporally as  $f_{\tau+1} \sim \mathbb{F}(f_\tau, \eta_\tau)$ , where  $\mathbb{F}$  is a distribution varying with time  $\tau$  and exogenous inputs  $\eta$ . Our approach builds on the fact that in several cases, temporal evolution  
5 can be hierarchically separated from spatial functional evolution. A classical and quite general example of this is the *abstract evolution equation* (AEO), which can be defined as the evolution of a function  $u$  embedded in a Banach space  $\mathcal{B}$ :  $\dot{u}(t) = \mathcal{L}u(t)$ , subject to  $u(0) = u_0$ , and  $\mathcal{L} : \mathcal{B} \rightarrow \mathcal{B}$  determines spatiotemporal transitions of  $u \in \mathcal{B}$  [32]. This model of spatiotemporal evolution is very general (AEOs, for example, model many PDEs), but working in Banach spaces  
10 can be computationally taxing. A simple way to make the approach computationally realizable is to place restrictions on  $\mathcal{B}$ : in particular, we restrict the sequence  $f_\tau$  to lie in a reproducing kernel Hilbert space (RKHS), the theory of which provides powerful tools for generating flexible classes of functions with relative ease [3]. In a kernel-based model,  $k : \Omega \times \Omega \rightarrow \mathbb{R}$  is a positive-definite Mercer kernel on a domain  $\Omega$  that models the covariance between any two points in  
15 the input space, and implies the existence of a smooth map  $\psi : \Omega \rightarrow \mathcal{H}$ , where  $\mathcal{H}$  is an RKHS with the property  $k(x, y) = \langle \psi(x), \psi(y) \rangle_{\mathcal{H}}$ . The key insight behind the proposed model is that spatiotemporal evolution in the input domain corresponds to temporal evolution of the mixing weights of a kernel model alone in the functional domain. Therefore,  $f_\tau$  can be modeled by tracing the evolution of its mean embedded in a RKHS using switched ordinary differential  
20 equations (ODE) when the evolution is continuous, or switched difference equations when it is discrete (Figure 3). The advantage of this approach is that it allows us to utilize powerful ideas from systems theory for deriving necessary and sufficient conditions for spatiotemporal monitoring.

In this paper, we restrict our attention to the class of functional evolutions  $\mathbb{F}$  defined by  
25 linear Markovian transitions in an RKHS. While extension to the nonlinear case is possible (and non-trivial), it is not pursued in this paper to help ease the exposition of the key ideas. The class of linear transitions in RKHS is rich enough to approximately model many real-world datasets, as suggested by our experiments.

Let  $y \in \mathbb{R}^N$  be the measurements of the function available from  $N$  sensors,  $\mathcal{A} : \mathcal{H} \rightarrow \mathcal{H}$  be a linear transition operator in the RKHS  $\mathcal{H}$ , and  $\mathcal{K} : \mathcal{H} \rightarrow \mathbb{R}^N$  be a linear measurement operator. The model for the functional evolution and measurement studied in this paper is:

$$f_{\tau+1} = \mathcal{A}f_\tau + \eta_\tau, \quad y_\tau = \mathcal{K}_\tau f_\tau + \zeta_\tau, \quad (1)$$

where  $\eta_\tau$  is a zero-mean stochastic process in  $\mathcal{H}$ , and  $\zeta_\tau$  is a Wiener process in  $\mathbb{R}^N$ . Classical  
30 treatments of kernel methods emphasize that for most kernels, the feature map  $\psi$  is unknown, and possibly infinite-dimensional; this forces practitioners to work in the dual space of  $\mathcal{H}$ , whose

dimensionality is the number of samples in the dataset being modeled. This conventional wisdom precludes the use of kernel methods for most tasks involving modern datasets, which may have millions and sometimes billions of samples [33]. An alternative is to work with a feature map  $\widehat{\psi}(x) := [\widehat{\psi}_1(x) \dots \widehat{\psi}_M(x)]^T$  to an approximate feature space  $\widehat{\mathcal{H}}$ , with the property that for every 5 element  $f \in \mathcal{H}$ ,  $\exists \widehat{f} \in \widehat{\mathcal{H}}$  and an  $\epsilon > 0$  s.t.  $\|f - \widehat{f}\| < \epsilon$  for an appropriate function norm. A few such approximations are listed below.

*Dictionary of atoms:* Let  $\Omega$  be compact. Given points  $\mathcal{C} = \{c_1, \dots, c_M\}$ ,  $c_i \in \Omega$ , we have a dictionary of atoms  $\mathcal{F}^{\mathcal{C}} = \{\psi(c_1), \dots, \psi(c_M)\}$ ,  $\psi(c_i) \in \mathcal{H}$ , the span of which is a strict subspace  $\widehat{\mathcal{H}}$  of the RKHS  $\mathcal{H}$  generated by the kernel. Here,

$$\widehat{\psi}_i(x) := \langle \psi(x), \psi(c_i) \rangle_{\mathcal{H}} = k(x, c_i). \quad (2)$$

10 *Low-rank approximations:* Let  $\Omega$  be compact, let  $\mathcal{C} = \{c_1, \dots, c_M\}$ ,  $c_i \in \Omega$ , and let  $K \in \mathbb{R}^{M \times M}$ ,  $K_{ij} := k(c_i, c_j)$  be the Gram matrix computed from  $\mathcal{C}$ . This matrix can be diagonalized to compute approximations  $(\widehat{\lambda}_i, \widehat{\phi}_i(x))$  of the eigenvalues and eigenfunctions  $(\lambda_i, \phi_i(x))$  of the kernel [34]. These spectral quantities can then be used to compute  $\widehat{\psi}_i(x) := \sqrt{\widehat{\lambda}_i} \widehat{\phi}_i(x)$ .

15 *Random Fourier features:* Let  $\Omega \subset \mathbb{R}^n$  be compact, and let  $k(x, y) = e^{-\|x-y\|^2/2\sigma^2}$  be the Gaussian RBF kernel. Then random Fourier features approximate the kernel feature map as  $\widehat{\psi}_{\omega} : \Omega \rightarrow \widehat{\mathcal{H}}$ , where  $\omega$  is a sample from the Fourier transform of  $k(x, y)$ , with the property that  $k(x, y) = \mathbb{E}_{\omega}[\langle \widehat{\psi}_{\omega}(x), \widehat{\psi}_{\omega}(y) \rangle_{\widehat{\mathcal{H}}}]$  [33]. In this case, if  $V \in \mathbb{R}^{M/2 \times n}$  is a random matrix representing the sample  $\omega$ , then  $\widehat{\psi}_i(x) := [\frac{1}{\sqrt{M}} \sin([Vx]_i), \frac{1}{\sqrt{M}} \cos([Vx]_i)]$ . Similar approximations exist for other radially symmetric kernels, as well as dot-product kernels.

In the approximate space case, we replace the transition operator  $\mathcal{A} : \mathcal{H} \rightarrow \mathcal{H}$  in (1) by  $\widehat{\mathcal{A}} : \widehat{\mathcal{H}} \rightarrow \widehat{\mathcal{H}}$ . This approximate regime, which combines the flexibility of a truly nonparametric approach with computational realizability, still allows for the representation of rich phenomena, as will be seen in the sequel, and in Figure 5. The finite-dimensional evolution equations approximating (1) in dual form are

$$w_{\tau+1} = \widehat{A}w_{\tau} + \eta_{\tau}, \quad y_{\tau} = Kw_{\tau} + \zeta_{\tau}, \quad (3)$$

20 where we have matrices  $\widehat{A} \in \mathbb{R}^{M \times M}$ ,  $K \in \mathbb{R}^{N \times M}$ , the vectors  $w_{\tau} \in \mathbb{R}^M$ , and where we have slightly abused notation to let  $y_{\tau}, \eta_{\tau}$  and  $\zeta_{\tau}$  denote their  $\widehat{\mathcal{H}}$  counterparts. Here  $K$  is the matrix whose rows are of the form  $K_{(i)} = \widehat{\Psi}(x_i) = [\widehat{\psi}_1(x_i) \ \widehat{\psi}_2(x_i) \ \dots \ \widehat{\psi}_M(x_i)]$ . In systems-theoretic language, each row of  $K$  corresponds to a *measurement* at a particular location, and the matrix itself acts as a measurement operator.

The equations (1) suggest an immediate extension to functional control problems. Pick another basis for  $\mathcal{H}$  as  $\widetilde{\psi}(x) := [\widetilde{\psi}_1(x) \ \dots \ \widetilde{\psi}_{\ell'}(x)]^T$ , where the functions  $\widetilde{\psi}_j(x)$  are

used to approximate the RKHS  $\mathcal{H}$  generated by the kernel. We denote the span of these functions as  $\tilde{\mathcal{H}}$ . In the dictionary of atoms case, an example would be another set of atoms  $\mathcal{F}_D = [\psi(d_1) \ \dots \ \psi(d_{\ell'})]$ ,  $\psi(d_j) \in \mathcal{H}$ ,  $d_j \in \Omega$ , with  $\tilde{\mathcal{H}}$  being a strict subspace of the RKHS  $\mathcal{H}$  generated by the kernel. The functional evolution equation is then as follows:

$$f_{\tau+1} = \mathcal{A}f_\tau + \mathcal{B}\delta_\tau + \eta_\tau, \quad y_\tau = \mathcal{K}_\tau f_\tau + \zeta_\tau, \quad (4)$$

where the control functions  $\delta_\tau$  evolve in  $\tilde{\mathcal{H}}$ , and  $\mathcal{B} : \tilde{\mathcal{H}} \rightarrow \widehat{\mathcal{H}}$ . To derive the finite-dimensional equivalent of  $\mathcal{B}$ , we have to work out the structure of the matrix  $B$ : since  $\widehat{\mathcal{H}}$  is not, in general, isomorphic to  $\tilde{\mathcal{H}}$ , this imposes strict restrictions on  $B$ . We can derive  $B$  using least squares using the inner product of  $\mathcal{H}$ . An instructive example is where both  $\widehat{\mathcal{H}}$  and  $\tilde{\mathcal{H}}$  are generated by dictionaries of atoms; recall that in this case,  $\mathcal{F}^C = [\psi(c_1) \ \dots \ \psi(c_M)]$  is the basis for  $\widehat{\mathcal{H}}$ , and let  $\delta = \sum_{j=1}^{\ell'} \dot{w}_j \psi(d_j)$ , and let  $\mathcal{F}^C = [\psi(c_1) \ \dots \ \psi(c_M)]$  be the basis for  $\mathcal{H}^C$ . Then the projection of  $\delta$  onto  $\widehat{\mathcal{H}}$  can be derived as

$$\begin{bmatrix} \langle \delta, \psi(c_1) \rangle_{\mathcal{H}} \\ \vdots \\ \langle \delta, \psi(c_M) \rangle_{\mathcal{H}} \end{bmatrix} = \underbrace{\begin{bmatrix} \langle \psi(d_1), \psi(c_1) \rangle_{\mathcal{H}} & \dots & \langle \psi(d_{\ell'}), \psi(c_1) \rangle_{\mathcal{H}} \\ \vdots & \ddots & \vdots \\ \langle \psi(d_1), \psi(c_M) \rangle_{\mathcal{H}} & \dots & \langle \psi(d_{\ell'}), \psi(c_M) \rangle_{\mathcal{H}} \end{bmatrix}}_{K_{CD}} \begin{bmatrix} \dot{w}_1 \\ \vdots \\ \dot{w}_{\ell'} \end{bmatrix}. \quad (5)$$

Note that in the dictionary of atoms case, the entries of  $K_{CD}$  can be computed in closed form as  $K_{CDij} := k(d_i, c_j)$ , using the reproducing property. This derivation shows that the operator  $B$  is simply  $K_{CD} \in \mathbb{R}^{M \times \ell'}$ , the kernel matrix between the data  $C$  generating the atoms  $\mathcal{F}^C$  of  $\widehat{\mathcal{H}}$  and the data  $D$  generating the atoms  $\mathcal{F}_D$  of  $\tilde{\mathcal{H}}$ . Thus, the finite-dimensional evolution equations equivalent to (4) are

$$w_\tau = \widehat{A}w_\tau + K_{CD}\dot{w}_\tau, \quad y_\tau = K_\tau w_\tau. \quad (6)$$

We define the *generalized observability matrix* [35] as  $\mathcal{O}_\Upsilon = \begin{bmatrix} K\widehat{A}^{\tau_1} \\ \vdots \\ K\widehat{A}^{\tau_L} \end{bmatrix}$  where  $\Upsilon = \{\tau_1, \dots, \tau_L\}$  are the set of instances  $\tau_i$  when we apply the operator  $K$ . A linear system is said to be *observable* if  $\mathcal{O}_\Upsilon$  has full column rank (i.e.  $\text{Rank}(\mathcal{O}_\Upsilon) = M$ ) for  $\Upsilon = \{0, 1, \dots, M-1\}$  [35]. Observability guarantees two critical facts: firstly, it guarantees that the state  $w_0$  can be recovered exactly from a finite series of measurements  $\{y_{\tau_1}, y_{\tau_2}, \dots, y_{\tau_L}\}$ ; in particular, defining  $y_\Upsilon = [y_{\tau_1}^T, y_{\tau_2}^T, \dots, y_{\tau_L}^T]^T$ , we have that  $y_\Upsilon = \mathcal{O}_\Upsilon w_0$ . Secondly, it guarantees that a feedback based *observer* can be designed such that the estimate of  $w_\tau$ , denoted by  $\widehat{w}_\tau$ , converges exponentially fast to  $w_\tau$  in the limit of samples. Note that all our theoretical results assume  $\widehat{A}$  is available: while we perform system identification in the experiments ([18]), it is not the focus of the paper.

We are now in a position to formally state the spatiotemporal modeling, control, and inference problems being considered: given a spatiotemporally evolving system modeled using (3), choose a set of  $N$  sensing locations such that even with  $N \ll M$ , the functional evolution

of the spatiotemporal model can be estimated (which corresponds to *monitoring*), can be predicted robustly (which corresponds to *Bayesian filtering*), and which can be controlled (which corresponds to *functional control*). Our approach to solve the monitoring and prediction problem relies on the design of the measurement operator  $K$  so that the pair  $(K, \hat{A})$  is observable:

5 any Bayesian state estimator (e.g. a Kalman filter) utilizing this pair is denoted as a **kernel observer**<sup>2</sup>. In the controls case, given a spatiotemporally evolving system modeled using (6), we need to choose a set of  $N$  sensing locations and  $\ell'$  control locations, such that even with  $N \ll M$ ,  $\ell' \ll M$ , the functional evolution of the spatiotemporal model can be controlled; in this case, we must design both a measurement operator  $K$  and a control operator  $K_{CD}$  such

10 that the pair  $(K_{CD}, \hat{A})$  is controllable: a controls system utilizing this pair and the measurement operator  $K$  is denoted as a **kernel controller**.

## Preliminaries on Rational Canonical Structures

We take a geometric approach towards the choice of sampling locations for inferring  $w_\tau$  in (3); the extension for control is similar. We use the notation  $\mathcal{V}$ , with  $\dim(\mathcal{V}) = M$ , to emphasize the fact that these theorems hold for any finite-dimensional vector space. Consider the linear operator  $\mathcal{A} : \mathcal{V} \rightarrow \mathcal{V}$ , and recall that the definition of observability requires the construction of a linear operator  $\mathcal{K} : \mathcal{V} \rightarrow \mathcal{U}$ , with  $\dim(\mathcal{U}) = N$ , such that  $\text{rank}[(\mathcal{K})^T \dots (\mathcal{K}\mathcal{A}^{M-1})^T]^T = M$ . In most applications, if  $N \geq M$ , and  $\text{rank } \mathcal{K} = N$ , it is reasonable to expect that observability may be achieved. However, for our purposes,  $N$  must be *significantly* less than  $M$ . Therefore,

20 we must design  $\mathcal{K}$  with as small a rank as possible. To do so, we require a series of vectors  $v_i$  that, under repeated iterations of  $\mathcal{A}$ , can generate a basis for  $\mathcal{V}$ . For this task, we will use a fundamental decomposition result from the theory of modules, known as the *rational canonical structure* of  $\mathcal{A}$  [36]. The intuition here is that if the sequence  $\{v_i\}_i$  can generate this basis, it can be directly used to construct  $\mathcal{K}$ .

The linear operator  $\mathcal{A} : \mathcal{V} \rightarrow \mathcal{V}$  has a characteristic polynomial  $\pi(\lambda)$  such that  $\pi(\mathcal{A}) = 0$  by the Cayley-Hamilton theorem. The minimal polynomial (MP) of  $\mathcal{A}$  is the monic polynomial  $\alpha(\cdot)$  of least degree (denoted by  $\deg(\cdot)$ ) given as  $\alpha(\lambda) = a_0 + a_1\lambda + \dots + \lambda^{\deg(\alpha)} = 0$ , such that  $\alpha(\mathcal{A}) = a_0I + a_1\mathcal{A} + \dots + \mathcal{A}^{\deg(\alpha)} = 0$ . The MP is unique and divides  $\pi(\lambda)$ , so that  $\deg(\alpha) \leq \deg(\pi)$ . The MP of a vector  $v \in \mathcal{V}$  relative to  $\mathcal{A}$  is the unique monic polynomial  $\xi_v$  of least degree such that  $\xi_v(\mathcal{A})v = a_0v + a_1\mathcal{A}v + \dots + \mathcal{A}^{\deg(\alpha)}v = 0$ . If  $\deg(\alpha) = M$ , then  $\mathcal{A}$  is *cyclic* and  $\exists v \in \mathcal{V}$ , such that the vectors  $\{v, \mathcal{A}v, \dots, \mathcal{A}^{M-1}v\}$  form a basis for  $\mathcal{V}$ ; this is the same as saying that the pair  $(v^T, \mathcal{A}^T)$  is observable. A subspace  $\mathcal{V}_S \subset \mathcal{V}$  s.t.  $\mathcal{A}\mathcal{V}_S \subset \mathcal{V}_S$  is  $\mathcal{A}$ -*cyclic*

<sup>2</sup>In the case where no measurements are taken, for the sake of consistency, we denote the state estimator as an **autonomous kernel observer**, despite this being somewhat of an oxymoron.

if  $\mathcal{A}|_{\mathcal{V}_S}$ , the restriction of  $\mathcal{A}$  to the subspace  $\mathcal{V}_S$ , is cyclic. If  $\alpha(\lambda)$  is the minimal polynomial of  $\mathcal{A}$  and  $\deg(\alpha) = m < M$ ,  $\exists v \in \mathcal{V}$  such that  $\{v, \mathcal{A}v, \dots, \mathcal{A}^{m-1}v\}$  span an  $m$ -dimensional  $\mathcal{A}$ -cyclic subspace  $\mathcal{V}_S$ , with  $v$  being the *cyclic generator* of  $\mathcal{V}_S$ . The subspace  $\mathcal{V}_S$  decomposes  $\mathcal{V}$  relative to  $\mathcal{A}$ . By the rational canonical structure theorem (Theorem 0.1 of [36]),  $\mathcal{A}$  can be 5 successively decomposed into subspaces  $\mathcal{V}_i \subset \mathcal{V}$ ,  $i \in \{1, \dots, \ell\}$ , s.t.  $\mathcal{V} = \mathcal{V}_1 \oplus \dots \oplus \mathcal{V}_\ell$ ,  $\mathcal{A}\mathcal{V}_i \subset \mathcal{V}_i$ , and  $\mathcal{A}|_{\mathcal{V}_i}$ ,  $i \in \{1, \dots, \ell\}$ , are cyclic<sup>3</sup>. The integer  $\ell$  is unique and is called the *cyclic index of  $\mathcal{A}$* .

One of our main results is to show that the cyclic index is a lower bound on the number of measurements required to reconstruct  $w_\tau$  (see Prop. 3 and Alg. 1 in [18]). The matrix transform associated to this theorem is known as the *Frobenius normal form* (denoted by  $C \in \mathbb{R}^{M \times M}$ ): 10 for  $\mathcal{A} \in \mathbb{R}^{M \times M}$ ,  $\exists Q \in \mathbb{R}^{M \times M}$  invertible such that  $\mathcal{A} = QCQ^{-1}$ . We will also use the *Jordan decomposition*, where for  $\mathcal{A} \in \mathbb{R}^{M \times M}$ ,  $\exists P \in \mathbb{R}^{M \times M}$  invertible such that  $\mathcal{A} = P\Lambda P^{-1}$ , where  $\Lambda$  is a unique block diagonal matrix with Jordan blocks with  $\lambda_i$  along the diagonal. If all the eigenvalues  $\lambda_i$  are nonzero and real, we say the matrix has a *full-rank Jordan decomposition*.

## Main Results

15 In this section, we prove results concerning the observability of spatiotemporally varying functions modeled by the functional evolution and measurement equations (3). In particular, observability of the system states implies that we can recover the current state of the spatiotemporally varying function using a small number of sampling locations  $N$ , which allows us to 1) track the function, and 2) predict its evolution forward in time. We work with the 20 approximation  $\widehat{\mathcal{H}} \approx \mathcal{H}$ : given  $M$  basis functions, this implies that the dual space of  $\widehat{\mathcal{H}}$  is  $\mathbb{R}^M$ . Proposition 1 shows that if  $\widehat{\mathcal{A}}$  has a full-rank Jordan decomposition, the observation matrix  $K$  meeting a condition called *shadedness* (Definition 1) is sufficient for the system to be observable. Proposition 2 provides a lower bound on the number of sampling locations required 25 for observability which holds for any  $\widehat{\mathcal{A}}$ . Proposition 3 constructively shows the existence of an abstract measurement map  $\widetilde{K}$  achieving this lower bound. Since the measurement map does not have the structure of a kernel matrix, a slightly weaker sufficient condition for the observability of any  $\widehat{\mathcal{A}}$  is in Theorem 1. Finally, since both  $K$  and  $K_{CD}$  are kernel matrices generated from a shared kernel, these observability results translate directly into controllability results. Proofs of all claims are in the appendix.

30 **Definition 1: (Shaded Observation Matrix)** Given  $k : \Omega \times \Omega \rightarrow \mathbb{R}$  positive-definite on a domain  $\Omega$ , let  $\{\widehat{\psi}_1(x), \dots, \widehat{\psi}_M(x)\}$  be the set of bases generating an approximate feature map  $\widehat{\psi} : \Omega \rightarrow \widehat{\mathcal{H}}$ , and let  $\mathcal{X} = \{x_1, \dots, x_N\}$  be the set of sampling (or sensing) locations, with each  $x_i \in \Omega$ . Let  $K \in \mathbb{R}^{N \times M}$  be the observation matrix, where  $K_{ij} := \widehat{\psi}_j(x_i)$ . For each

<sup>3</sup>In general, the subspaces  $\mathcal{V}_i$  are not unique for a fixed  $\mathcal{A}$ .

row  $K_{(i)} := [\widehat{\psi}_1(x_i) \dots \widehat{\psi}_M(x_i)]$ , define the set  $\mathcal{I}_{(i)} := \{\iota_1^{(i)}, \iota_2^{(i)}, \dots, \iota_{M_i}^{(i)}\}$  to be the indices in the observation matrix row  $i$  which are nonzero. Then if  $\bigcup_{i \in \{1, \dots, N\}} \mathcal{I}^{(i)} = \{1, 2, \dots, M\}$ , we denote  $K$  as a *shaded observation matrix* (see Figure 4a).

This definition seems quite abstract, so the following remark considers a more concrete

5 example.

*Remark 1:* let  $\widehat{\psi}$  be generated by the dictionary given by  $\mathcal{C} = \{c_1, \dots, c_M\}$ ,  $c_i \in \Omega$ . Note that since  $\widehat{\psi}_j(x_i) = \langle \psi(x_i), \psi(c_j) \rangle_{\mathcal{H}} = k(x_i, c_j)$ ,  $K$  is the kernel matrix between  $\mathcal{X}$  and  $\mathcal{C}$ . For the kernel matrix to be shaded thus implies that there does not exist an atom  $\psi(c_j)$  such that the projections  $\langle \psi(x_i), \psi(c_j) \rangle_{\mathcal{H}}$  vanish for all  $x_i$ ,  $1 \leq i \leq N$ . Intuitively, the shadedness property 10 requires that the sensor locations  $x_i$  are privy to information propagating from every  $c_j$ . As an example, note that, in principle, for the Gaussian kernel, a single row generates a shaded kernel matrix<sup>4</sup>.

*Proposition 1:* Given  $k : \Omega \times \Omega \rightarrow \mathbb{R}$  positive-definite on a domain  $\Omega$ , let  $\{\widehat{\psi}_1(x), \dots, \widehat{\psi}_M(x)\}$  be the set of bases generating an approximate feature map  $\widehat{\psi} : \Omega \rightarrow \widehat{\mathcal{H}}$ , 15 and let  $\mathcal{X} = \{x_1, \dots, x_N\}$ ,  $x_i \in \Omega$ . Consider the discrete linear system on  $\widehat{\mathcal{H}}$  given by the evolution and measurement equations (3). Suppose that a full-rank Jordan decomposition of  $\widehat{A} \in \mathbb{R}^{M \times M}$  of the form  $\widehat{A} = P\Lambda P^{-1}$  exists, where  $\Lambda = [\Lambda_1 \dots \Lambda_O]$ , and there are no repeated eigenvalues. Then, given a set of time instances  $\Upsilon = \{\tau_1, \tau_2, \dots, \tau_L\}$ , and a set of sampling 20 locations  $\mathcal{X} = \{x_1, \dots, x_N\}$ , the system (3) is observable if the observation matrix  $K_{ij}$  is shaded according to Definition 1,  $\Upsilon$  has distinct values, and  $|\Upsilon| \geq M$ .

When the eigenvalues of the system matrix are repeated, it is not enough for  $K$  to be shaded. In the next proposition, we take a geometric approach and utilize the rational canonical form of  $\widehat{A}$  to obtain a lower bound on the number of sampling locations required. Let  $r$  be the number of unique eigenvalues of  $\widehat{A}$ , and let  $\gamma_{\lambda_i}$  denote the geometric multiplicity of eigenvalue 25  $\lambda_i$ . Then the *cyclic index* of  $\widehat{A}$  is defined as  $\ell = \max_{1 \leq i \leq r} \gamma_{\lambda_i}$  [36].

*Proposition 2:* Suppose that the conditions in Proposition 1 hold, with the relaxation that the Jordan blocks  $[\Lambda_1 \dots \Lambda_O]$  may have repeated eigenvalues (i.e.  $\exists \Lambda_i$  and  $\Lambda_j$  s.t.  $\lambda_i = \lambda_j$ ). Then there exist kernels  $k(x, y)$  such that the lower bound  $\ell$  on the number of sampling locations  $N$  is given by the cyclic index of  $\widehat{A}$ . In other words, the system in (3) is observable if  $N \geq \ell$ .

30 We will give a concrete example to build intuition regarding this lower bound below. For

<sup>4</sup>However, in this case, the matrix can have many entries that are extremely close to zero, and will probably be very ill-conditioned.

now, we note the following:

*Proposition 3:* Given the conditions stated in Proposition 2, it is possible to construct a measurement map  $\tilde{K} \in \mathbb{R}^{\ell \times M}$  for the system given by (3), such that the pair  $(\tilde{K}, \hat{A})$  is observable.

The construction provided in the proof of Proposition 3 is utilized in Algorithm 1, which uses the rational canonical structure of  $\hat{A}$  to generate a series of vectors  $v_i \in \mathbb{R}^M$ , whose iterations  $\{v_1, \dots, \hat{A}^{m_1-1}v_1, \dots, v_\ell, \dots, \hat{A}^{m_\ell-1}v_\ell\}$  generate a basis for  $\mathbb{R}^M$ . Unfortunately, the measurement map  $\tilde{K}$ , being an abstract construction unrelated to the kernel, does not directly select  $\mathcal{X}$ . We will show how to use the measurement map to guide a search for  $\mathcal{X}$  in Remark 2 (in Appendix). For now, we state a sufficient condition for observability of a general system.

*Theorem 1:* Suppose that the conditions in Proposition 1 hold, with the relaxation that the Jordan blocks  $\begin{bmatrix} \Lambda_1 & \cdots & \Lambda_O \end{bmatrix}$  may have repeated eigenvalues. Let  $\ell$  be the cyclic index of  $\hat{A}$ . Define

$$\mathbf{K} = [K^{(1)T} \dots K^{(\ell)T}]^T \quad (7)$$

as the  $\ell$ -shaded matrix (see Figure 4b) which consists of  $\ell$  shaded matrices with the property that any subset of  $\ell$  columns in the matrix are linearly independent from each other. Then system (3) is observable if  $\Upsilon$  has distinct values, and  $|\Upsilon| \geq M$ .

While Theorem 1 is a quite general result, the condition that any  $\ell$  columns of  $\mathbf{K}$  be linearly independent is a very stringent condition. One scenario where this condition can be met with minimal measurements is in the case when the feature map  $\hat{\psi}(x)$  is generated by a dictionary of atoms with the Gaussian RBF kernel evaluated at sampling locations  $\{x_1, \dots, x_N\}$  according to (2), where  $x_i \in \Omega \subset \mathbb{R}^d$ , and  $x_i$  are sampled from a non-degenerate probability distribution on  $\Omega$  such as the uniform distribution. For a semi-deterministic approach, when the dynamics matrix  $\hat{A}$  is block-diagonal, we can utilize a simple heuristic:

*Remark 2:* Let  $\Omega$  be compact,  $\mathcal{C} = \{c_1, \dots, c_M\}$ ,  $c_i \in \Omega$ , and let the approximate feature map be defined by (2). Consider the system (3) with  $\hat{A} = \Lambda$ , and let  $\Upsilon = \{0, 1, \dots, M-1\}$ . Then the measurement map  $\tilde{K}$ 's values lie in  $\{0, 1\}$ ; in particular, each row  $\tilde{K}^{(j)}$ ,  $j \in \{1, \dots, \ell\}$ , corresponds to a subspace  $\hat{\mathcal{H}}_j$ , generated by a subset of centers  $\mathcal{C}^{(j)} \subset \mathcal{C}$ . Generate samples  $x_i^{(j)}$  to create a kernel matrix  $K^{(j)}$  that is shaded only with respect to centers  $\mathcal{C}^{(j)}$ . Once this is done, move on to the next subspace  $\hat{\mathcal{H}}_{j+1}$ . When all  $\ell$  rows of  $\tilde{K}$  are accounted for, construct the matrix  $\mathbf{K}$  as in (7). Then the resulting system  $(\mathbf{K}, \hat{A})$  is observable.

This heuristic is formalized in Algorithm 2. Note that in practice, the matrix  $\hat{A}$  needs to be inferred from measurements of the process  $f_\tau$ . If no assumptions are placed on  $\hat{A}$ , it's clear

that at least  $M$  sensors are required for the system identification phase. Future work will study the precise conditions under which system identification is possible with less than  $M$  sensors.

## Discussion of Theoretical Results

- The systems-theoretic approach taken in this paper reveals something rather surprising:
- 5 functions with complex dynamics (with a small cyclic index) can be recovered with less sensor placements than functions with simpler dynamics. Although seemingly counterintuitive, it becomes clear that this is because complex dynamics, which are characterized by a lower geometric multiplicity of the eigenvalues, ensure that the orbit  $\Theta := \{\widehat{A}w_\tau\}_{\tau \in \Upsilon}$  traverses a greater portion of  $\mathbb{R}^M \equiv \widehat{\mathcal{H}}$  and thus that fewer sensors can recover more geometric information.
  - 10 On the other hand, in ‘simpler’ functional evolution,  $\Theta$  evolves along strict subspaces of  $\mathbb{R}^M$ , and so more independent sensors are required to infer the same amount of information.

- In the case described in Remark 2, we have a set of centers  $\mathcal{C} = \{c_1, \dots, c_M\}$ , which generate the bases  $\mathcal{F}^{\mathcal{C}} = \{\psi(c_1), \dots, \psi(c_M)\}$ . Let the cyclic index be  $\ell$ : this implies that there exist  $\ell$  subsets  $\Psi^{(i)}$  of  $\mathcal{F}^{\mathcal{C}}$  with at least one element  $\psi(c_j)$  each, leading to  $\binom{M}{\ell}$  possible choices:
- 15 Figure 8 represents these choices as hyperplanes separating the subsets. The measurement map described in Alg. 1 in [18] induces this *decomposition of bases*  $\mathcal{F}^{\mathcal{C}} = \{\Psi^{(1)}, \dots, \Psi^{(\ell)}\}$  in polynomial time. Further, each subset  $\Psi^{(i)}$  is directly associated to a subset of centers  $\mathcal{C}^{(i)} \subset \mathcal{C}$ , which allows us to pick targeted sensor locations  $x_i \in \Omega$ . In particular, for radially symmetric kernels such as the Gaussian, the centroid of the convex hull of  $\mathcal{C}^{(i)}$  is sufficient for generating a
  - 20 sensor placement. The measurement map is a significant theoretical insight into sensor placement for dynamically changing environments, because it directly takes into account the dynamics of the process. Of course, in practice, this may be too expensive for approximate feature spaces with  $M$  very large, so one can use random sampling to generate the sensor locations instead, at the cost of  $N$  being larger than  $\ell$ . The advantage here though is that since random sampling
  - 25 is computationally inexpensive, different choices of sensor placements can be generated and evaluated relatively quickly.

- Another point to note is that since the collection of bases  $\{\widehat{\psi}_i(x)\}_{i=1}^M$  determines the richness of the function space  $\widehat{\mathcal{H}} \approx \mathcal{H}$  we operate in, it determines the fidelity of the model approximation to the true time-varying function. As a consequence, observability of the system in  $\widehat{\mathcal{H}}$  refers to the best possible approximation in  $\widehat{\mathcal{H}}$ . The greater the number of bases, the higher the dimensionality, which results in greater model fidelity, but which may require a much greater number of measurements for state recovery. This is where the lower bounds presented in the paper are particularly useful, because they show that for functional evolutions corresponding to certain  $\widehat{A}$ , *the number of sensor placements are essentially independent of the dimensionality*

$M$ , but depend rather on the cyclic index of  $\widehat{A}$ .

Figure 7 gives an overall picture on the process of generating a kernel observer, while Figure 8 gives two approaches to sensor selection in our framework. The measurement map approach can generate a smaller set of sensors than the random placement approach, but comes  
5 at an additional computational cost.

## Random Sensor Placement

We now elaborate on how the challenging problem of sensor placement can be tackled through random selection. This process of random selection is a product of the kernel observer model described above. We present the theoretical background required to prove Theorem 2,  
10 which states the expected number of randomly placed sensors required to monitor a given spatiotemporal process, and Theorem 3, which determines the probability with which optimal sensor placement is ensured given that,  $N$  number of sensors have been placed.

As discussed earlier, we work with an approximate feature space  $\widehat{\mathcal{H}}$ , with the corresponding transition operator  $\widehat{A} : \widehat{\mathcal{H}} \rightarrow \widehat{\mathcal{H}}$ , representing finite-dimensional functional evolution. To achieve  
15 observability for the pair  $(\widehat{A}, K)$ , row vectors of the corresponding observability matrix,  $\mathcal{O}$ , should form the basis for the  $\mathbb{R}^M$ -dimensional space  $\widehat{\mathcal{H}}$ . According to the rational canonical structure Theorem [36],  $\widehat{A}$  can successively decompose the dual space  $\mathbb{R}^M$  into subspaces,  $\mathcal{V}_i \subset \mathcal{V}$ ,  $i \in \{1, \dots, \ell\}$ , with properties, i)  $\mathcal{V} = \mathcal{V}_1 \oplus \dots \oplus \mathcal{V}_\ell$ , ii)  $\widehat{A}\mathcal{V}_i \subset \mathcal{V}_i$ , and iii)  $\widehat{A}|_{\mathcal{V}_i}, i \in \{1, \dots, \ell\}$ , are cyclic. The integer  $\ell$  is unique and is called the *cyclic index of  $\widehat{A}$* . Each of these  
20 properties contribute towards the theorem on the number of random samples required to achieve observability. The first property shows that the space  $\mathbb{R}^M$  can be decomposed into  $\ell$  independent subspaces. The second property shows that the vector  $v_i \in \mathcal{V}_i$  stays in  $\mathcal{V}_i$  even when operated upon by  $\widehat{A}$ . Thus, to generate bases for  $\mathbb{R}^M$ , one needs at least  $\ell$  vectors, say,  $v_1, \dots, v_\ell$ , with respect to each subspace  $\mathcal{V}_1, \dots, \mathcal{V}_\ell$ . This holds due to the third property, but requires that the  
25 vectors  $v_1, \dots, v_\ell$ , are the cyclic generators of their corresponding subspaces. Our analysis is based on whether a randomly selected sensor can generate a cyclic generator. To examine this, recall that a row vector  $K_{(i)}$  generated by a randomly selected sensor location  $x_i$  takes the form,

$$K_{(i)} = \left[ k(x_i, c_1), \dots, k(x_i, c_M) \right]. \quad (8)$$

Here, for radial kernels for example, the entries corresponding to the centers closer to  $x_i$  tend to  
30 be non-zero, whereas the others tend to be zero. The rows  $K_{(i)}$  from random sensor placement must be able to generate a basis for a subspace  $\mathcal{V}_i$ , and thus must be cyclic generators. We will derive the expected number of random sensor placements sufficient for observability for the case where  $\widehat{A} = \Lambda$  and then attempt to generalize the result for any  $\widehat{A}$ . Note  $\Lambda$  is a block diagonal

Jordan form. In this case, the cyclic generator for each subspace  $\mathcal{V}_i$ , is a vector  $v_i$  with non-zero entries corresponding to the leading entry of the Jordan blocks of  $\mathcal{V}_i$ .

Overall, our construction is as follows: for each subspace  $\mathcal{V}_i$ , let  $\mathcal{C}_{\mathcal{V}_i} \subset \mathcal{C}$  be the centers corresponding to those leading entry of Jordan blocks: then the minimum number of random samples required to generate the bases for  $\mathcal{V}_i$  is equal to the number of Jordan blocks comprising  $\mathcal{V}_i$ . Altogether, the minimum number of random samples required to generate a basis for  $\mathbb{R}^M$  is equal to the total number of Jordan blocks in  $\widehat{A}$ . Let  $\varsigma$  be the total number of Jordan blocks in  $\widehat{A}$ , then

$$\varsigma = \sum_{\lambda \in \sigma(\widehat{A})} \gamma_{\widehat{A}}(\lambda) \quad (9)$$

where  $\sigma(\widehat{A})$  represents the spectrum of  $\widehat{A}$ , whose elements are the eigenvalues of  $\widehat{A}$ , and  $\gamma_{\widehat{A}}(\lambda)$  is the geometric multiplicity corresponding to the eigenvalue  $\lambda$ , which is also equal to the total number of Jordan blocks corresponding to the eigenvalue  $\lambda$ . Define a set of centers  $\mathcal{C}_\varsigma$  with elements  $\{c_1, c_2, \dots, c_\varsigma\}$ , to be the centers corresponding to the leading entries of the Jordan blocks. For sensor location  $x \in \Omega$ , and  $\epsilon > 0$ , let  $k(x, c_j) > \epsilon$ , denote the region  $\Omega_j \subset \Omega$ , such that the kernel evaluation with respect to center  $c_j$  is greater than  $\epsilon$ , that is  $\Omega_j \equiv \{x \in \Omega : k(x, c_j) > \epsilon\}$ . We define  $p_\epsilon$  as

$$p_\epsilon = \min_{c_j \in \mathcal{C}_\varsigma} \frac{\nu(k(x, c_j) > \epsilon)}{\nu(\Omega)}, \quad (10)$$

where  $\nu$  is a measure in the real analysis sense. Hence,  $p_\epsilon$  corresponds to a lower bound on the probability that a random sample lies within the  $\epsilon$ -shaded region of a particular center  $c_j$ . With all of this in place, we can prove the following theorem.

*Theorem 2:* Given the spatiotemporal function  $f(x, \tau)$  with  $x \in \Omega \subseteq \mathbb{R}^D, \tau \in \mathbb{Z}^+$  its kernel observer model (3), and a tolerance parameter  $\epsilon > 0$ , the expected number of randomly placed sensor locations required to achieve observability for the pair  $(K, \widehat{A})$  is  $\varsigma/p_\epsilon$  where  $\varsigma$  is the summation over geometric multiplicities of each  $\lambda \in \sigma(\widehat{A})$  given by Equation (9).

*Theorem 3:* Given the spatiotemporal function  $f(x, \tau)$  with  $x \in \Omega \subseteq \mathbb{R}^D, \tau \in \mathbb{Z}^+$ , its kernel observer model (3), a tolerance parameter  $\epsilon > 0$ , summation over geometric multiplicities of each  $\lambda \in \sigma(\widehat{A})$  denoted by  $\varsigma$  as in Equation (9), and a constant  $\delta \in (0, 1]$ , the probability that pair  $(K, \widehat{A})$  is unobservable after the selection of  $N$  random sensors is at most  $e^{-\frac{1}{2}(Np_\epsilon - 2\varsigma)}$ , where  $p_\epsilon$  is given by Equation (10) and  $N \geq \varsigma/p_\epsilon$ .

For the case when  $\widehat{A} \neq \Lambda$ , a change of basis can be used to obtain  $\Lambda = P^{-1}\widehat{A}P$ , where  $P$  is the projection map. There are two challenges in performing the above analysis for  $\Lambda$  so obtained: first, the leading entries of Jordan blocks do not directly correspond to the centers  $\{c_1, \dots, c_M\}$

which was the case for  $\widehat{A} = \Lambda$ . Second, although we can obtain the transformation of the row vector (Equation (8)) using the projection map  $P$ , we can no longer arrive at the definition of the probability  $p_\epsilon$  as in Equation (10). The existence of the similarity transform hints that the results in Theorems 2-3 should hold for any  $\widehat{A}$ , but the mathematical tools utilized in the paper seem to be insufficient to prove them. However, we present some empirical evidence for these claims for when  $\widehat{A} \neq \Lambda$  in Section [22].

## Generalizing Across Similar Spatiotemporally Evolving Systems

Building on the Kernel Observers method, let us introduce Evolving Gaussian Processes (E-GP). The primary novelty in this method of generating a model is learning an  $\widehat{A}$  matrix for *multiple* systems. The ultimate goal of this research would be to generate highly efficient machine learning models that can be used instead of the costly numerical simulations for design and autonomy purposes. This would be a major success for the design and control of complex physical systems, such as soft robotics, as they would significantly reduce the cost and resources required in simulations. The ability to generalize across different physical situations, is critical. This is a difficult problem, as it requires that the model have the capability to actually learn the underlying physics and not just input-output relationships. For example, in the context of fluid flows, these models must be able to predict fluid dynamics at different conditions (e.g. Reynolds number) than the training data. E-GP, as far as the authors know, was the first machine learning method to generalize across spatiotemporally evolving systems of such complexity using end-to-end data.

We found that the class of functional evolutions  $\mathbb{F}$  defined by linear Markovian transitions in a RKHS is still sufficient to model the nonlinear Navier Stokes equations which govern fluid dynamics, since the unknown map  $\psi$  allows us to model highly nonlinear dynamics in the input space. However, we do expect that phenomena such as bifurcation or turbulence will require nonlinear mappings  $\mathcal{H}$ . There are three steps to generate an E-GP model:

- 1) After picking the kernel and estimating the bandwidth hyperparameter  $\sigma$  (we utilize the maximum likelihood approach, although other approaches can be used), find an optimal basis vector set  $\mathcal{C}$  using the algorithm in [37].
- 2) Use Gaussian process inference to find weight vectors for each time-step in the training set(s), generating the sequence  $w_\tau, \tau = 1, \dots, T$  for each system. A uniform time-step makes next step easier but can be worked around for non-uniform data sets
- 3) Using the weight trajectory, use matrix least-squares with the equation  $\widehat{A}[w_1, w_2, \dots, w_{T-1}] = [w_2, w_3, \dots, w_T]$  to solve for  $\widehat{A}$ .
- 4) To generate a multi-system model, concatenate the weight trajectories from each similar

system in the least-squares computation of  $\hat{A}$ . That is, let  $W_\theta = [w_1^{(\theta)}, w_2^{(\theta)}, \dots, w_{n-1}^{(\theta)}]$  and  $W'_\theta = [w_2^{(\theta)}, w_3^{(\theta)}, \dots, w_n^{(\theta)}]$  be the weight trajectory and next weight trajectory for some parameter  $\theta$ . Then we solve the least-squares problem  $\hat{A} = [W_{\theta_1}, \dots, W_{\theta_n}] = [W'_\theta, \dots, W'_{\theta_n}]$

For the sake of defining when it is appropriate to expect this method to be able to generalize across different spatiotemporally evolving systems, we shall define what it means for two fluid flows to be *similar*. In configuring a fluid dynamics simulation, a set of quantifiable parameters are defined. Two dynamical fluid systems  $S_1$  and  $S_2$  are considered *similar* if they have the same configuration of parameters and differ only in the value of at most one parameter. Furthermore, we require that the parameter be continuously variable, and that any observable quantity in the domain of the system vary smoothly as that parameter varies from its value in  $S_1$  to its value in  $S_2$ . For example, for fluids flowing past identical cylinders, the Reynolds number associated with the free stream velocity may be varied to produce similar systems. However, to replace the system's cylinder with a triangle would be to qualitatively change the configuration of the system parameters, and thus would produce a non-similar system.

Unlike neural networks, the weights in an E-GP do not exist in some abstract, difficult-to-comprehend space, but are associated with kernel centers in specific locations in the domain. We refer to this attribute of E-GPs as the *spatial encoding* property. This property is an extremely valuable tool for gaining insight into the learned model works:

- 1) By plotting which kernel centers are associated with which invariant subspaces in the transition matrix, one can visualize where the eigenfunctions are found and how the dynamic modes are separated spatially
- 2) By plotting arrows from center  $c_j$  to  $c_i$  for each of the largest elements  $\hat{a}_{ij}$  of  $\hat{A}$ , one can visualize how different areas of the domain influence each other's evolution.
- 3) By performing an eigendecomposition of the  $\hat{A}$  matrix, and transforming the eigenvectors back from the weight space to the function space, one can obtain the Koopman modes (and associated eigenvalues) of the system.

## Empirical Results

### Sensing Locations for Synthetic Data Sets

The goal of this experiment is to investigate the dependency of the observability of system (3) on the shaded observation matrix and the lower bound presented in Proposition 2. The domain is fixed on the interval  $\Omega = [0, 2\pi]$ . First, we pick sets of points  $\mathcal{C}^{(i)} = \{c_1, \dots, c_{M_i}\}$ ,  $c_j \in \Omega$ ,  $M = 50$ , and construct a dynamics matrix  $A = \Lambda \in \mathbb{R}^{M \times M}$ , with cyclic index 5. We pick the RBF kernel  $k(x, y) = e^{-\|x-y\|^2/2\sigma^2}$ ,  $\sigma = 0.02$ . Generating samples  $\mathcal{X} = \{x_1, \dots, x_N\}$ ,  $x_i \in \Omega$

randomly, we compute the  $\ell$ -shaded property and observability for this system. Figure 9a shows how shadedness is a necessary condition for observability, validating Proposition 1: the slight gap between shadedness and observability here can be explained due to numerical issues in computing the rank of  $\mathcal{O}_\Upsilon$ .

5 Next, we consider a system with a cyclic index  $\ell = 18$  to verify random sensor placement results. We constructed the measurement operator  $K$  using the heuristic in Remark 2 (Algorithm 2), and random sensor selection to generate the sampling locations  $\mathcal{X}$ . These results are presented in Figure 9b. The plot for random sampling which has been averaged over 100 runs, resembles a c.d.f function of an exponential distribution  $F(X = x) = 1 - \exp(-\lambda x)$ . This verifies the claim  
10 made in Theorem 3, as the probability of becoming unobservable decays exponentially with the number of sensors placed. Also, fitting an exponential distribution we found that the mean  $\lambda^{-1}$  comes close to the ratio  $\varsigma/p$ , which is the expected number of randomly placed sensors required for observability as per Theorem 2. Note that observability is not achieved if the number of samples  $N < \ell$  verifying the result in Proposition 2.

## 15 Comparison With Nonstationary Kernel Methods on Real-World Data

We use three real-world datasets to evaluate and compare the kernel observer with the two different lines of approach for non-stationary kernels discussed in Section . For the Process Convolution with Local Smoothing Kernel (PCLSK) and Latent Extension of Input Space (LEIS) approaches, we compare with NOSTILL-GP [6] and [29] respectively, on the Intel Berkeley, Irish  
20 Wind and Ozone data-sets.

Model inference for the kernel observer involved three steps: 1) picking the Gaussian RBF kernel  $k(x, y) = e^{-\|x-y\|^2/2\sigma^2}$ , a search for the ideal  $\sigma$  is performed for a sparse Gaussian Process model (with a fixed basis vector set  $\mathcal{C}$  selected using the method in [37]. For the data set discussed in this section, the number of basis vectors were equal to the number of sensing locations in  
25 the training set, with the domain for input set defined over  $\mathbb{R}^2$ ; 2) having obtained  $\sigma$ , Gaussian process inference is used to generate weight vectors for each time-step in the training set, resulting in the sequence  $w_\tau, \tau \in \{1, \dots, T\}$ ; 3) matrix least-squares is applied to this sequence to infer  $\hat{A}$  (Algorithm 3). For prediction in the autonomous setup,  $\hat{A}$  is used to propagate the state  $w_\tau$  forward to make predictions with no feedback, and in the observer setup, a Kalman  
30 filter (Algorithm 4) with  $N$  determined using Proposition 2, and locations picked randomly, is used to propagate  $w_\tau$  forward to make predictions. We also compare with a baseline GP (denoted by ‘original GP’), which is the sparse GP model trained using all of the available data.

Our first dataset, the Intel Berkeley research lab temperature data, consists of 50 wireless temperature sensors in indoor laboratory region spanning 40.5 meters in length and 31 meters in

width<sup>5</sup>. Training data consists of temperature data on March 6th 2004 at intervals of 20 minutes (beginning 00:20 hrs) which totals to 72 timesteps. Testing is performed over another 72 timesteps beginning 12:20 hrs of the same day. Out of 50 locations, we uniformly selected 25 locations each for training and testing purposes. Results of the prediction error are shown in box-plot form  
5 in Figure 10a and as a time-series in Figure 10b, note that ‘Auto’ refers to autonomous set up. Here, the cyclic index of  $\hat{A}$  was determined to be 2, so  $N$  was set to 2 for the kernel observer with feedback. Note that here, even the autonomous kernel observer outperforms PCLSK and LEIS overall, and the kernel observer with feedback with  $N = 2$  significantly outperforms all other methods, which is why we did not include results with  $N > 2$ .

10 The second dataset is the Irish wind dataset, consisting of daily average wind speed data collected from year 1961 to 1978 at 12 meteorological stations in the Republic of Ireland<sup>6</sup>. The prediction error is in box-plot form in Figure 11a and as a time-series in Figure 11b. Again, the cyclic index of  $\hat{A}$  was determined to be 2. In this case, the autonomous kernel observer’s performance is comparable to PCLSK and LEIS, while the kernel observer with feedback with  
15  $N = 2$  again outperforms all other methods.

Finally, the Ozone dataset measures ozone concentration (in parts per billion) measured at 60 stations by the United States Environmental Protection Agency [38] across USA. Due to missing measurements, we only selected data from year 1997 to 2013 for training and evaluation. For each station, we averaged ozone concentration over a period of three months, resulting in  
20 four quarters per year. Out of 60 sensor locations, we uniformly selected 30 for training and the remaining locations for testing purposes. The prediction error results are presented in box-plot form in Figure 12a and as a time-series in Figure 12b. Here, the cyclic index of  $\hat{A}$  was determined to be 1. In this case, the performance of autonomous kernel observer is comparable to PCLSK and LEIS, with kernel observer with feedback with  $N = 1$  performing the best. Table 1 reports  
25 the total training and prediction times associated with PCLSK, LEIS, and the kernel observer. We observed that, 1) the kernel observer is an order of magnitude faster than the competing methods, and 2) even for small sets, competing methods did not scale well.

## Prediction of Global Ocean Surface Temperature

We analyzed the feasibility of our approach on a very large dataset from the National  
30 Oceanographic Data Center: the 4 km AVHRR Pathfinder project, which is a satellite monitoring global ocean surface temperature (Figure 13a shows raw satellite data). This dataset is challenging, with measurements at over 37 million possible coordinates, but with only around 3-4

<sup>5</sup><http://db.csail.mit.edu/labdata/labdata.html>

<sup>6</sup><http://lib.stat.cmu.edu/datasets/wind.desc>

million measurements available per day, leading to a lot of missing data. The goal was to learn the day and night temperature models on data from the year 2011, and then to monitor thereafter for 2012. Success in monitoring would demonstrate two things: 1) the modeling process can capture spatiotemporal trends that generalize across years, and 2) the observer framework allows us to infer the state using a number of measurements that are an order of magnitude fewer than available. Note that due to the size of the dataset and the high computational requirements of the nonstationary kernel methods, a comparison with them was not pursued. To build the autonomous kernel observer and general kernel observer models, we followed the same procedure outlined in Section , but with  $\mathcal{C} = \{c_1, \dots, c_M\}$ ,  $c_j \in \mathbb{R}^2$ ,  $|\mathcal{C}| = 300$ . The Kalman filter for the general kernel observer model used  $N \in \{250, 500, 1000\}$  at random locations to track the system state given a random initial condition  $w_0$ . As a fair baseline, the observers are compared to training a sparse GP model (labeled ‘original’) on approximately 400,000 measurements per day. Figure 13b is an estimate of global ocean surface temperatures obtained using autonomous kernel observer. Figures 13c and 13d compare the autonomous and feedback approach with 1,000 samples to the baseline GP; here, it can be seen that the autonomous does well in the beginning, but then incurs an unacceptable amount of error when the time series goes into 2012, i.e. where the model has not seen any training data, whereas FKO does well throughout. Figures 13e and 13f show a comparison of the RMS error of estimated values from the real data. This figure shows the trend of the observer getting better and better state estimates as a function of the number of sensing locations  $N$ <sup>7</sup>. Time required for kernel observer is much lesser than retraining the model every time step, see figures 13g-13h.

**Weather Anomaly in 2012:** We further investigated the poor performance of autonomous kernel observer in the year 2012 as observed in Figures 13c and 13d. Clearly, the error in prediction blows up at the start of May in the year 2012. Indicating that the autonomous model trained using the data of the year 2011 does well in capturing the annual weather dynamics up to the month of May 2012. We turned our attention towards the weather in May 2012, as changes in ocean temperatures are directly related to the weather. Surprisingly, severe weather onset was reported on the east coast of United States in May 2012, and this anomaly continued over the period of May to June 2012. Thus, the apparent poor performance of autonomous kernel observer can actually be a useful indicator in detecting the anomalous behavior, as was the case with the ocean temperature in May 2012 which had deviated from the nominal weather dynamics observed in the year 2011 in which no severe weather anomalies were reported. Further, we identified the locations at which the prediction error was two standard deviations above the mean error. These error locations are plotted in Figure 14. Error locations on 6-7th May coincide with the severe

<sup>7</sup>Note that we checked the performance of training a GP with only 1,000 samples as a control, but the average error was about 10 Kelvins, i.e. much worse than FKO.

weather onset on the east coast of United states and that of 28-29th May were along the track of storm Beryl approaching the eastern coastline. This shows that the autonomous kernel observer model captures the dynamics of spatiotemporal evolution, and has the potential of identifying current behavior as anomalous to that observed in the training set.

## 5 Predicting evolution of weed density in agricultural fields

As a proof-of-concept in applying our methods for learning dynamics and/or inferring the state of spatiotemporally-evolving systems to real, relevant problems, we present our work with weed growth in agricultural fields.

Past work has presented detailed analysis of weed growth models, in which measurements 10 of seed bank density for various species of weeds were conducted [39]–[42]. In order to generate data upon which to test our methods, we implemented a weed growth simulation model whose rate of seedling emergence agrees with that found in the above research. A Poisson process is utilized to simulate the temporal evolution of emergence events. This assumption is reasonable over the short time scales in which robots may fully weed a field.

15 Other work in the field of crop science [43], [44] has shown that the spatial variation in the seed bank density for some species of weeds may be modeled via the Gini Coefficient of Concentration (GCC). This model is accurate for common waterhemp (*Amaranthus tuberculatus*), and thus we found it useful in our simulation of the spatial distribution of the seed bank density. For more reading, see [45], [46] regarding the relationship between seed bank emergence patterns 20 and environmental conditions such as temperature and moisture.

The weed growth simulation is based on Bernoulli random variables, operating on a matrix of cells, each  $0.8 \text{ m}^2$ , comprising a gridded field of 0.4 hectares, or a cellular automata model [47]. Seeds emerge from a limited seed bank, forming a binomial distribution over time. The parameters used, summarized in Table 2, are aligned with the growth model for common 25 waterhemp determined in [43]. The initial density of the seed bank in each cell is  $S_0$  on average (between 600 and 1560 seeds per cell). However, at the start of the simulation, the seed bank density in each cell,  $S_0(x, y)$ , is chosen so that Gini Coefficient of Concentration (GCC) between all the cells, used to ensure the relative density of weeds aligns with that seen in real experiments, is from 0.31 to 0.35, as was determined experimentally in [43]. The field is first divided into 30 fifty patches of weeds, with centers chosen uniformly at random, and sizes from zero to twenty cells in each dimension. Each cell has an initial density between zero and twenty percent of  $S_0$ , chosen uniformly at random. Finally, for each patch of weeds, up to an additional  $S_0$  weeds are added to each cell within each patch, so that the density of each patch follows a normal

distribution.

Upon initialization of the simulation, a certain number of days,  $d_0$ , are allowed to elapse before weeding starts. The number of emerging weeds in each cell,  $N_{\text{emerge}}$ , is a randomly generated Poisson variable with mean,  $\lambda(x, y, t)$ , such that 90 percent of the seed bank,  $S(x, y, t)$ , emerges in  $T_{\text{total}}$ , which is two months. This emergence rate is aligned with past work [39]–[42], [46], which all present measurements of the seed bank densities for various species of weeds, and provide an analysis of weed growth models for these species.

The weed density in each cell,  $\zeta(x, y, t)$ , grows as seeds emerge from the seed bank. The maximum weed height at each cell,  $\delta(x, y, t)$ , increases from zero height at a fixed rate  $\Gamma$  inches per day.

Of course, robots going out to weed a field only have access to sparse data about weed density and height, and no data about the seedbank or about the field in locations that have not been visited. For this reason, we have trained a Kernel observers model on the weed density data generated by our simulations, so that robots in the field can quickly infer the state of the field globally from sparse measurements.

We used a Radial Basis Function (RBF) kernels with a bandwidth approximately 5 cells (4.5 meters) wide. These were centered throughout the domain using Csato & Opper’s algorithm. After training a GP on each snapshot of the data, we obtained a weight vector trajectory. We used linear least squares do determine the best linear transition in the weight space for this trajectory. Below we have included images of system as predicted by feeding forward the initial condition through this linear transition, as a comparison with the original data. The model is able to approximate the weed density growth data very well, with percent error averaging 5%.

## Control of a linear PDE

We then employed kernel controllers for controlling an approximation to the scalar diffusion equation  $u_t = bu_{xx}$  on the domain  $\Omega = [0, 1]$ , with  $b = 0.25$ . The solution to this equation is infinite-dimensional, so we chose a kernel  $k(x, y) = e^{-(\|x-y\|^2/2\sigma^2)}$ , and a set of atoms  $\mathcal{F}^C = \{c_1, \dots, c_M\}$ ,  $c_i \in \Omega$ , with  $M = 25$  generating  $\mathcal{H}^C$ , the space approximating  $\mathcal{H}$ , and another set of atoms  $\mathcal{F}_D = \{\psi(d_1), \dots, \psi(d_{\ell'})\}$ ,  $d_j \in \Omega$ ,  $\ell' = 13$ , generating the control space  $\tilde{\mathcal{H}}$ . The number of, and the location of the observations was chosen to be the same as that of the actuation locations  $d_j$ . First, tests (not reported here) were conducted to ensure that the solution to the diffusion equation is well approximated in  $\mathcal{H}^C$ . Matrix least-squares was used to infer  $\hat{A}$ . Figure 16a shows an example of an initial function  $f_{\text{init}}$  evolving according to the PDE. A reference function  $f_{\text{ref}} \in \mathcal{H}^C$  was chosen to drive  $f_{\text{init}}$  to  $f_{\text{ref}}$  under the action of the PDE. Finally,

Algorithm 5 was used to control the PDE, driving  $f_{\text{init}}$  to  $f_{\text{ref}}$ ; Figure 16b shows the absolute value of the error between  $f_k$  and  $f_{\text{ref}}$  as a function of time.

## Conclusion

Machine learning techniques such as Gaussian Process regression and deep learning are providing increasingly more powerful ways of learning predictive models. However, these techniques are limited by the datasets that they are trained with. Hence, their predictions are not always reliable when predicting real-world complex spatiotemporally-evolving phenomena with lots of variability. Indeed, years worth of weather data cannot be a reliable predictor of weather, nor can data from one farm directly relate to another. Hence, when engineering complex cyber-physical systems such as team of mechanically weeding robots, engineers have to think of ways to supplement the predictions of the machine learning models with real measurements. However, this is not always immediate when one works in the abstract feature spaces utilized in machine learning models. Here we presented Evolving Gaussian Processes, which are formed by embedding a linear dynamical system in the reproducing kernel Hilbert spaces generated by the Gaussian Process model. The parameters of the linear dynamical system can be trained to approximately predict the evolution. In itself this can lead to powerful and generalizable models, as our results demonstrated in predicting solutions to the Navier-Stokes equations. Furthermore, a Kalman filter can be embedded with the linear dynamical system in the RKHS that can keep the predictions on track with real sensor measurements. This creates a very powerful prediction system that is capable of predicting nonlinear evolution using very few sensor measurements. We showed that the geometric properties of the linear dynamical system can be utilized to determine sensor numbers and locations. Looking forward, it would be interesting to extend the idea to include nonlinear dynamical systems in the feature space. Such embeddings could improve the capability of the E-GP model. However, it seems from our results with complex datasets that the feedback with sensors creates a robust monitoring system with the predictions with a simple linear model. The theoretical limits of the tradeoff between improving the model versus increasing the sensing in the context of E-GPs is interesting to study. Finally, also we note that deep neural networks have also been applied to the spatiotemporal modeling problem with significant empirical success [48], but because these methods are 1) nonlinear in their parameters, and 2) lack the spatial-encoding properties of some types of kernels, they are less amenable to analysis for the tasks we consider here. Yet, as sidebar *Feature Spaces in Machine Learning* indicates, there could be very interesting future work in this area.

## Software

To facilitate implementation of the material presented in this paper we have made an open-source code-base. A MATLAB version is available at <http://daslab.illinois.edu/software.html> or at <https://github.com/hkingravi/FunctionObservers> with examples and documentation. In addition,  
5 a Python version is available on GitHub at <https://github.com/hkingravi/funcobspy>.

## ACKNOWLEDGMENTS

The work presented was supported in part by AFOSR #FA9550-15-1-0146, and USDA/NSF  
CPS grant 2018-67007-28379. We thank EarthSense Inc. ([www.earthsense.co](http://www.earthsense.co)) for providing us  
with Figures 1 and S1. The authors also thank Prof. Stephen Long and Prof. Carl Bernacchi on  
10 insights about the phenotyping bottleneck and simulation of plants (*crops-in-silico*), Prof. Adam  
Davis on inputs on the herbicide-resistant weed crisis, and Prof. Sarah Lovell and Dr. Chinmay  
Soman on sustainable agricultural production systems and perennial polycultures. We also thank  
the members of the UIUC Center for Digital Agriculture for their inputs.

## References

- [1] Wyatt McAllistar, Denis Osipychev, Girish Chowdhary, and Adam Davis. Multi-agent planning for coordinated robotic weed killing. In *International Conference on Intelligent Robots and Systems (IROS)*, Madrid, Spain, 2018. IEEE.
- [2] Noel Cressie and Christopher K Wikle. *Statistics for spatio-temporal data*. John Wiley & Sons, 2011.
- [3] Carl E. Rasmussen and Christopher K. I. Williams. *Gaussian Processes for Machine Learning*. The MIT Press, December 2005.
- [4] K.-R. Müller, S. Mika, G. Rätsch, S. Tsuda, and B Schölkopf. An introduction to kernel-based learning algorithms. *IEEE Transactions on Neural Networks*, 12(2):181–202, 2001.
- [5] Bernhard Schölkopf and Alexander J Smola. *Learning with kernels: Support vector machines, regularization, optimization, and beyond*. MIT press, 2002.
- [6] Sahil Garg, Amarjeet Singh, and Fabio Ramos. Learning non-stationary space-time models for environmental monitoring. In *Proceedings of the Twenty-Sixth AAAI Conference on Artificial Intelligence, July 22-26, 2012, Toronto, Ontario, Canada.*, 2012.
- [7] Chunsheng Ma. Nonstationary covariance functions that model space–time interactions. *Statistics & Probability Letters*, 61(4):411–419, 2003.
- [8] Christian Plagemann, Kristian Kersting, and Wolfram Burgard. Nonstationary gaussian process regression using point estimates of local smoothness. In *Machine learning and knowledge discovery in databases*, pages 204–219. Springer, 2008.
- [9] G. Chowdhary, H. Kingravi, J.P. How, and P. Vela. Nonparametric adaptive control using gaussian processes. In *IEEE Conference on Decision and Control (CDC)*. IEEE, 2013.
- [10] Suvrit Sra, Sebastian Nowozin, and Stephen J Wright. *Optimization for machine learning*. Mit Press, 2012.
- [11] Sadeep Jayasumana, Richard Hartley, Mathieu Salzmann, Hongdong Li, and Mehrtash Harandi. Kernel Methods on Riemannian Manifolds with Gaussian RBF Kernels. *IEEE Transactions on Pattern Analysis and Machine Intelligence (TPAMI)*, 2015.
- [12] A. Gelb. *Applied Optimal Estimation*. MIT press (QA402.A5), Cambridge, MA, 1974.
- [13] Kanti V Mardia, Colin Goodall, Edwin J Redfern, and Francisco J Alonso. The kriged kalman filter. *Test*, 7(2):217–282, 1998.
- [14] F. Cucker and S. Smale. On the mathematical foundations of learning. *Bulletin of the American Mathematical Society*, 39(1), 2002.
- [15] Hassan A Kingravi, Girish Chowdhary, Patricio A Vela, and Eric N. Johnson. Reproducing kernel hilbert space approach for the online update of radial bases in neuro-adaptive control. *Neural Networks and Learning Systems, IEEE Transactions on*, 23(7):1130–1141, 2012.
- [16] M. Liu, G. Chowdhary, B. Castra da Silva, S. Liu, and J. P. How. Gaussian processes for

- learning and control: A tutorial with examples. *IEEE Control Systems Magazine*, 38(5):53–86, Oct 2018.
- [17] Carl Edward Rasmussen. Gaussian processes for machine learning. Technical report, Max Planck Institute for Biological Cybernetics, 2006.
- 5 [18] Hassan Kingravi, Harshal Maske, and Girish Chowdhary. Kernel observers: Systems theoretic modeling and inference of spatiotemporally varying processes. In *Advances in Neural Information Processing Systems (NIPS)*, Barcelona, Spain, 2016.
- 10 [19] Joshua Whitman, Harshal Maske, Girish Chowdhary, Hassan Kingravi, Chen Lu, and Balaji Jayaraman. Modeling nonlinear dynamical fluid flows with evolving gaussian process models. In *NIPS workshop on Machine Learning in the Wild*, Barcelona, Spain, 2016. NIPS.
- [20] Hassan A. Kingravi, Harshal Maske, and Girish Chowdhary. Kernel controllers: A systems-theoretic approach for data-driven modeling and control of spatiotemporally evolving processes. *arXiv*, abs/1508.02086, 2015.
- 15 [21] Joshua Whitman and Girish Chowdhary. Learning dynamics across similar spatiotemporally-evolving physical systems. In *Conference on Robot Learning*, pages 472–481, 2017.
- [22] Harshal Maske, Hassan Kingravi, and Girish Chowdhary. Sensor selection via observability analysis in feature space. In *American Control Conference*, 2018. accepted.
- 20 [23] Christopher K Wikle. A kernel-based spectral model for non-gaussian spatio-temporal processes. *Statistical Modelling*, 2(4):299–314, 2002.
- [24] Fernando Pérez-Cruz, Steven Van Vaerenbergh, Juan José Murillo-Fuentes, Miguel Lázaro-Gredilla, and Ignacio Santamaría. Gaussian processes for nonlinear signal processing: An overview of recent advances. *Signal Processing Magazine, IEEE*, 30(4):40–50, 2013.
- 25 [25] David Higdon. A process-convolution approach to modelling temperatures in the north atlantic ocean. *Environmental and Ecological Statistics*, 5(2):173–190, 1998.
- [26] C Paciorek and M Schervish. Nonstationary covariance functions for gaussian process regression. *Advances in neural information processing systems*, 16:273–280, 2004.
- 30 [27] Amarjeet Singh, Fabio Ramos, H Durrant-Whyte, and William J Kaiser. Modeling and decision making in spatio-temporal processes for environmental surveillance. In *Robotics and Automation (ICRA), 2010 IEEE International Conference on*, pages 5490–5497. IEEE, 2010.
- [28] Alexandra M Schmidt and Anthony O’Hagan. Bayesian inference for non-stationary spatial covariance structure via spatial deformations. *Journal of the Royal Statistical Society: Series B (Statistical Methodology)*, 65(3):743–758, 2003.
- 35 [29] Tobias Pfingsten, Malte Kuss, and Carl Edward Rasmussen. Nonstationary gaussian process regression using a latent extension of the input space. URL <http://www.kyb.mpg.de/>

- tpfingst*, 2006.
- [30] Mehran Mesbahi and Magnus Egerstedt. *Graph Theoretic Methods in Multiagent Networks*. Princeton University Press, 2010.
- [31] C. Guestrin, A. Krause, and A. Singh. Near-optimal sensor placements in gaussian processes. In *International Conference on Machine Learning*, 2005.
- [32] Haim Brezis. *Functional analysis, Sobolev spaces and partial differential equations*. Springer Science & Business Media, 2010.
- [33] Ali Rahimi and Benjamin Recht. Random features for large-scale kernel machines. In *NIPS*, pages 1177–1184, 2007.
- [34] Christopher Williams and Matthias Seeger. Using the Nyström method to speed up kernel machines. In *NIPS*, pages 682–688, 2001.
- [35] Kemin Zhou, John C. Doyle, and Keith Glover. *Robust and Optimal Control*. Prentice Hall, Upper Saddle River, NJ, 1996.
- [36] W Murray Wonham. *Linear multivariable control*. Springer, 1974.
- [37] Lehel Csatö and Manfred Opper. Sparse on-line gaussian processes. *Neural computation*, 14(3):641–668, 2002.
- [38] Lixin Li, Xingyou Zhang, and Reinhard Piltner. A spatiotemporal database for ozone in the conterminous us. In *Thirteenth International Symposium on Temporal Representation and Reasoning (TIME’06)*, pages 168–176. IEEE, 2006.
- [39] D. Nordby, R. Hartzler, and K. Bradley. Biology and management of waterhemp. *Glyphosate, Weeds, and Crop Sciences, Purdue University Extension, publication GWC-13.12*, 2007.
- [40] Brian J Schutte and Adam S Davis. Do common waterhemp (*amaranthus rudis*) seedling emergence patterns meet criteria for herbicide resistance simulation modeling? *Weed Technology*, 28(2):408–417, 2014.
- [41] Brent A Sellers, Reid J Smeda, William G Johnson, J Andrew Kendig, and Mark R Ellersieck. Comparative growth of six amaranthus species in Missouri. *Weed Science*, 51(3):329–333, 2003.
- [42] Michael J Horak and Thomas M Loughin. Growth analysis of four amaranthus species. *Weed Science*, 48(3):347–355, 2000.
- [43] Dawit Mulugeta and David E Stoltenberg. Seed bank characterization and emergence of a weed community in a moldboard plow system. *Weed Science*, pages 54–60, 1997.
- [44] Dawit Mulugeta and Chris M Boerboom. Seasonal abundance and spatial pattern of *setaria faberi*, *chenopodium album*, and *abutilon theophrasti* in reduced-tillage soybeans. *Weed science*, pages 95–106, 1999.
- [45] Adam S Davis, Sharon Clay, John Cardina, Anita Dille, Frank Forcella, John Lindquist, and Christy Sprague. Seed burial physical environment explains departures from regional

- hydrothermal model of giant ragweed (*ambrosia trifida*) seedling emergence in us midwest. *Weed science*, 61(3):415–421, 2013.
- [46] Rodrigo Werle, Lowell D Sandell, Douglas D Buhler, Robert G Hartzler, and John L Lindquist. Predicting emergence of 23 summer annual weed species. *Weed Science*, 2014.
- 5 [47] B Chopard and M Droz. *Cellular automata*. Springer, 1998.
- [48] Du Tran, Lubomir Bourdev, Rob Fergus, Lorenzo Torresani, and Manohar Paluri. Learning spatiotemporal features with 3d convolutional networks. In *Proceedings of the IEEE international conference on computer vision*, pages 4489–4497, 2015.
- 10 [49] Timothy J Richards. Immigration reform and farm labor markets. *American Journal of Agricultural Economics*, 100(4):1050–1071, 2018.
- [50] Tom Hertz and Steven Zahniser. Is there a farm labor shortage? *American Journal of Agricultural Economics*, 95(2):476–481, 2013.
- [51] Julie Guthman. Paradoxes of the border: labor shortages and farmworker minor agency in reworking californias strawberry fields. *Economic Geography*, 93(1):24–43, 2017.
- 15 [52] C. Morris. California crops rot as immigration crackdown creates farmworker shortage. *Fortune*, pages Online: <http://fortune.com/2017/08/08/immigration-worker-shortage-rotting-crops/>, 2017.
- [53] Alejandro Plastina. Estimated costs of crop production in iowa, 2018. *Iowa State University Extension & Outreach*, 2018.
- 20 [54] Adinor José Capelesso, Ademir Antonio Cazella, Abdon Luiz Schmitt Filho, Joshua Farley, and Diego Albino Martins. Economic and environmental impacts of production intensification in agriculture: comparing transgenic, conventional, and agroecological maize crops. *Agroecology and Sustainable Food Systems*, 40(3):215–236, 2016.
- [55] Jonathan A Foley, Navin Ramankutty, Kate A Brauman, Emily S Cassidy, James S Gerber, Matt Johnston, Nathaniel D Mueller, Christine OConnell, Deepak K Ray, Paul C West, Christian Balzer, Elena M. Bennett, Stephen R. Carpenter, Jason Hill, Chad Monfreda, Stephen Polasky, Johan Rockstrm, John Sheehan, Stefan Siebert, David Tilman, and David P. M. Zaks. Solutions for a cultivated planet. *Nature*, 478(7369):337–342, 2011.
- 25 [56] H. Charles J. Godfray, John R. Beddington, Ian R. Crute, Lawrence Haddad, David Lawrence, James F. Muir, Jules Pretty, Sherman Robinson, Sandy M. Thomas, and Camilla Toulmin. Food security: The challenge of feeding 9 billion people. *Science*, 327(5967):812–818, 2010.
- [57] I Heap. International survey of herbicide resistant weeds. <http://www.weedscience.org>, 2017.
- 30 [58] Michael Livingston, Jorge Fernandez-Cornejo, and George B Frisvold. Economic returns to herbicide resistance management in the short and long run: The role of neighbor effects. *Weed Science*, 64(sp1):595–608, 2016.

- [59] L. P. Gianessi and N. P. Reigner. The value of herbicides in us crop production. *Weed Technology*, 21(2):559–566, 2007.
- [60] Sarah Taylor Lovell, Christian Dupraz, Michael Gold, Shibu Jose, Ronald Revord, Erik Stanek, and Kevin J Wolz. Temperate agroforestry research: considering multifunctional woody polycultures and the design of long-term field trials. *Agroforestry Systems*, pages 1–19, 2017.
- [61] D. Mitchell. Labor shortage provides obstacle for berry growers. *The Packer*, July 26, 2017. 2017.
- [62] G. Mohan. As california’s labor shortage grows, farmers race to replace workers with robots. *Los Angeles Times*, July 21, 2017. 2017.
- [63] Erkan Kayacan, Zhongzhong Zhang, and Girish Chowdhary. Embedded high precision control and corn stand counting algorithms for an ultra-compact 3d printed field robot. *Proceedings of Robotics: Science and Systems. Pittsburgh, Pennsylvania*, 2018.
- [64] Tim Mueller-Sim, Merritt Jenkins, Justin Abel, and George Kantor. The robotanist: a ground-based agricultural robot for high-throughput crop phenotyping. In *IEEE International Conference on Robotics and Automation (ICRA), Singapore, Singapore*, 2017.
- [65] Nicolas Virlet, Kasra Sabermanesh, Pouria Sadeghi-Tehran, and Malcolm J Hawkesford. Field scanalyzer: An automated robotic field phenotyping platform for detailed crop monitoring. *Functional Plant Biology*, 44(1):143–153, 2017.
- [66] Søren Marcus Pedersen, S Fountas, Henrik Have, and BS Blackmore. Agricultural robotssystem analysis and economic feasibility. *Precision agriculture*, 7(4):295–308, 2006.
- [67] James A Dewar. Perennial polyculture farming: seeds of another agricultural revolution? Technical report, RAND CORP SANTA MONICA CA, 2007.
- [68] Brenda B Lin. Resilience in agriculture through crop diversification: adaptive management for environmental change. *BioScience*, 61(3):183–193, 2011.
- [69] Lori Ann Thrupp. Linking agricultural biodiversity and food security: the valuable role of agrobiodiversity for sustainable agriculture. *International affairs*, 76(2):283–297, 2000.
- [70] Deborah K Letourneau, Inge Armbrecht, Beatriz Salguero Rivera, James Montoya Lerma, Elizabeth Jimenez Carmona, Martha Constanza Daza, Selene Escobar, Victor Galindo, Catalina Gutierrez, Sebastian Duque Lopez, et al. Does plant diversity benefit agroecosystems? a synthetic review. *Ecological applications*, 21(1):9–21, 2011.
- [71] Xin-Guang Zhu, Jonathan P Lynch, David S LeBauer, Andrew J Millar, Mark Stitt, and Stephen P Long. Plants in silico: why, why now and what?an integrative platform for plant systems biology research. *Plant, cell & environment*, 39(5):1049–1057, 2016.
- [72] Elke Stehfest, Maik Heistermann, Joerg A. Priess, Dennis S. Ojima, and Joseph Alcamo. Simulation of global crop production with the ecosystem model DayCent. *Ecological Modelling*, 209(2–4):203–219, December 2007.

- [73] Jonathan A. Foley, I. Colin Prentice, Navin Ramankutty, Samuel Levis, David Pollard, Steven Sitch, and Alex Haxeltine. An integrated biosphere model of land surface processes, terrestrial carbon balance, and vegetation dynamics. *Global Biogeochemical Cycles*, 10(4):603–628, December 1996.
- <sup>5</sup> [74] Christopher J. Kucharik. Evaluation of a process-based agro-ecosystem model (agro-IBIS) across the U.S. corn belt: Simulations of the interannual variability in maize yield. *Earth Interactions*, 7(14):1–33, December 2003.
- <sup>10</sup> [75] Mark A. Friedl, Damien Sulla-Menashe, Bin Tan, Annemarie Schneider, Navin Ramankutty, Adam Sibley, and Xiaoman Huang. MODIS collection 5 global land cover: Algorithm refinements and characterization of new datasets. *Remote Sensing of Environment*, 114(1):168–182, 2010.
- [76] M. A. Rodrigues, D. M. Lopes, M. S. Leite, and V. M. Tabuada. Calibration and application of FOREST-BGC in NorthWestern of portugal. In *EGU General Assembly Conference Abstracts*, volume 12, page 7270, 2010.
- <sup>15</sup> [77] L. Nunes, M. A. Rodrigues, and D. Lopes. Evaluation of the climate change impact on the productivity of portuguese pine ecosystems using the forest-BGC model. In *Advances in Meteorology, Climatology and Atmospheric Physics*, pages 655–661. Springer, 2013.
- [78] Frank Rosenblatt. The perceptron: a probabilistic model for information storage and organization in the brain. *Psychological review*, 65(6):386, 1958.
- <sup>20</sup> [79] Corinna Cortes and Vladimir Vapnik. Support-vector networks. *Machine learning*, 20(3):273–297, 1995.
- [80] Y. Bengio. Learning deep architectures for ai. *Foundations and Trends in Machine Learning*, 2:1–127, 2009.
- <sup>25</sup> [81] Ian Goodfellow, Yoshua Bengio, Aaron Courville, and Yoshua Bengio. *Deep learning*, volume 1. MIT press Cambridge, 2016.
- [82] Graham Burnett. The seven layers of the forest garden. [https://en.wikipedia.org/?title=Forest\\_gardening#/media/File:Forgard2-003.gif](https://en.wikipedia.org/?title=Forest_gardening#/media/File:Forgard2-003.gif). Accessed: Dec 2018.
- [83] Christopher J Rhodes. Feeding and healing the world: through regenerative agriculture and permaculture. *Science progress*, 95(4):345–446, 2012.
- <sup>30</sup> [84] Ronald L Panton. *Incompressible flow*. John Wiley & Sons, 2006.
- [85] A. Roshko. On the development of turbulent wakes from vortex streets. *California Institute of Technology*, Report 1191, 1954.
- [86] M. Braza, P.H.H.M. Chassaing, and H.H. Minh. Numerical study and physical analysis of the pressure and velocity fields in the near wake of a circular cylinder. *Journal of fluid mechanics*, 165(130), 1986.
- <sup>35</sup> [87] B.N. Rajani, A. Kandasamy, and S. Majumdar. Numerical simulation of laminar flow past a circular cylinder. *Applied Mathematical Modelling*, 33(3):1228–1247, 2009.

Table 1: Total training and prediction times for Figs. 10 and 11

	<b>Intel</b> Berkeley	<b>Irish</b> Wind	<b>Ozone</b>
<i>Data Size (bases-timesteps)</i>	25-72	12-36	30-68
Kernel Observer	2.1 sec	0.1 sec	1.61 sec
PCLSK	121.4 sec	7.0 sec	91.90 sec
LEIS	43.8 sec	2.8 sec	37.41 sec

Table 2: Seed Bank Density Parameters

<b>Parameter</b>	GCC	$S_0$ (seeds/cell)	Num. of Patches	Patch Size (Cells in X and Y)
<b>Range</b>	[0.31,0.35]	[600,1560]	50	[0,20]

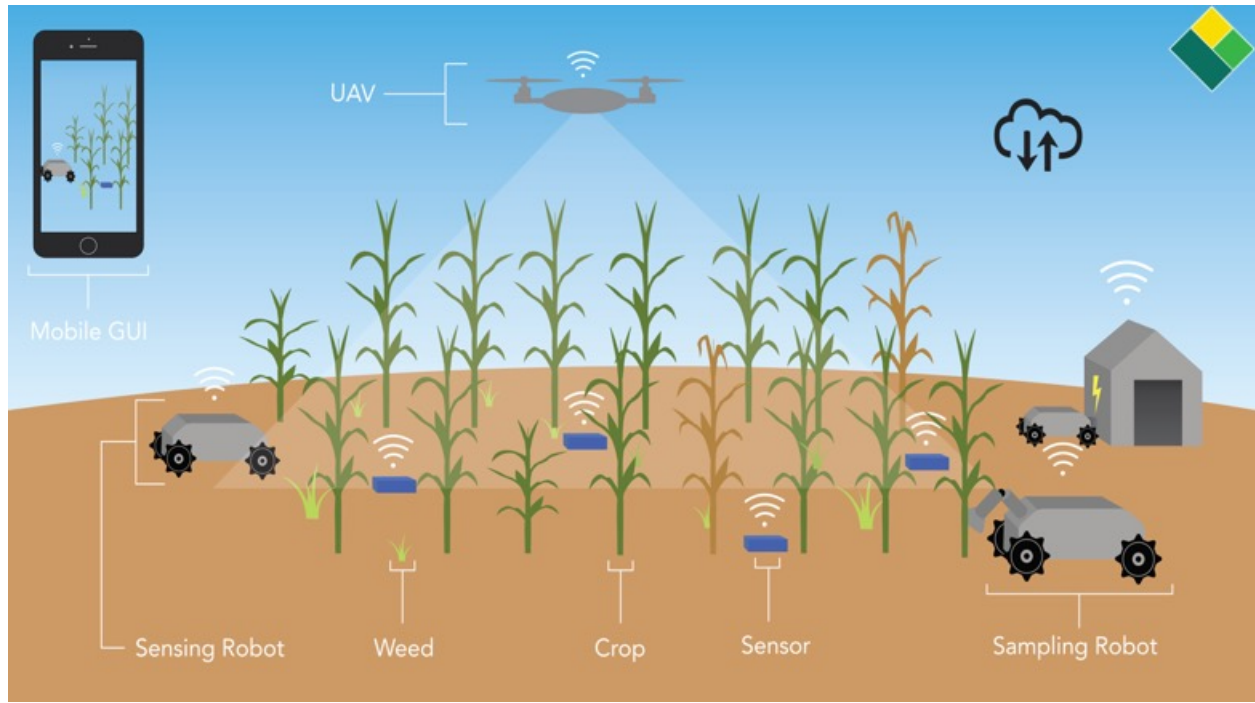


Figure 1: A Cyber Physical system consisting of a distributed team of robots for mechanical weed management on a farm. Image courtesy EarthSense inc.

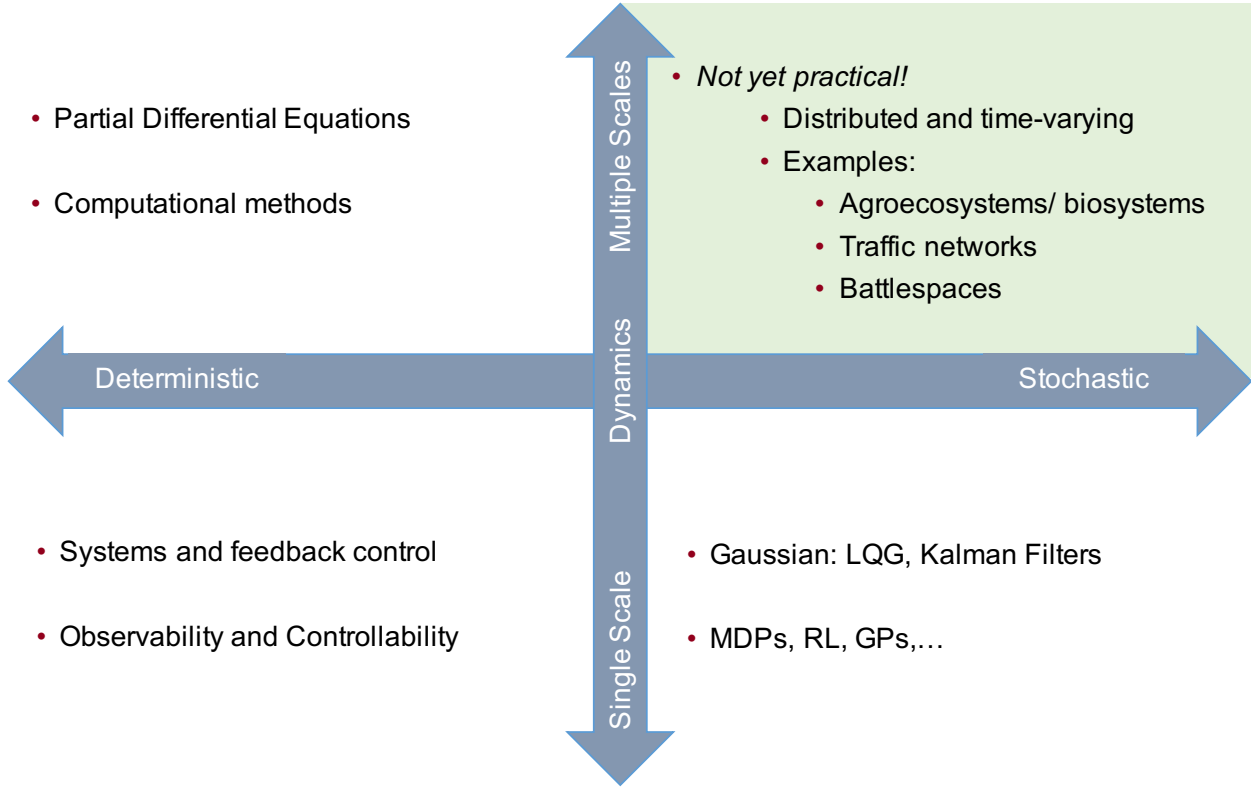
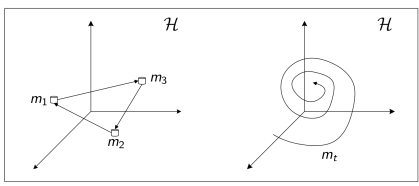
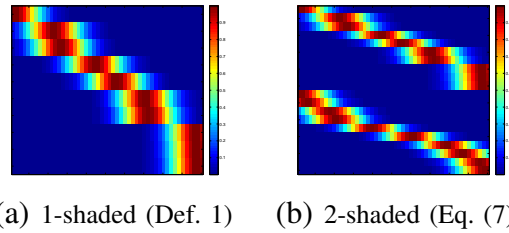


Figure 2: Modeling, monitoring, and controlling dynamical systems with complex and uncertain dynamics, such as agricultural, traffic, or weather monitoring systems, presents exciting open challenge for the controls community. The bottom left quadrant describes linear and time-invariant systems with single- scale dynamics, for which the theory of feedback control of dynamical systems is often sufficient. The bottom right quadrant shows stochastic single-scaled systems, where approaches such as Kalman Filters and Gaussian optimization have marked several successes of control systems enabling endeavors from Lunar landings to GPS navigation. The top left quadrant denotes systems with dynamics at multiple scales, where efficient computational solutions to Partial Differential Equations (PDEs) is an highly active area of research. However, fundamental theoretical advances and practical algorithms are needed to enable autonomous decision making for distributed stochastic Cyber Physical Systems with dynamics at multiple scales shown in the top right quadrant such as distributed agricultural robotic systems, traffic networks, and weather monitoring systems with mobile and stationary sensors.



**Figure 3:** Two types of Hilbert space evolutions. Left: discrete switches in RKHS  $\mathcal{H}$ ; Right: smooth evolution in  $\mathcal{H}$ .



**Figure 4:** Shaded observation matrices for dictionary of atoms. Each row represents a sensing location with the color map indicating the evaluation of kernel function w.r.t the others points in the domain.

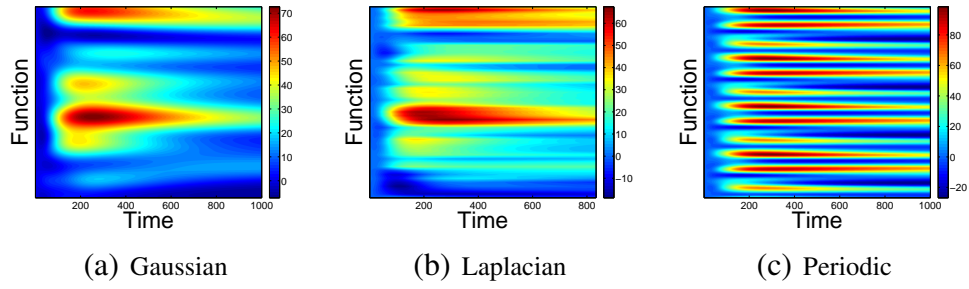


Figure 5: One-dimensional function evolution over a fixed transition matrix  $A$ , initial condition  $w_0$  and centers  $\mathcal{C}$ , but with different kernels  $k(x, y)$ . Each  $y$ -vector at a given value of  $x$  represents the output of the function, which evolves from left to right. As seen, changing the kernel creates quite different dynamic behaviors.

$$\begin{array}{ccc}
 \widehat{\mathcal{H}} & \xrightarrow{\mathcal{A}} & \widehat{\mathcal{H}} \\
 \mathcal{W} \downarrow & & \uparrow \mathcal{W}^{-1} \\
 \mathbb{R}^M & \xrightarrow{A} & \mathbb{R}^M
 \end{array}
 \quad
 \begin{array}{ccc}
 \widehat{\mathcal{H}} & \xrightarrow{\mathcal{K}} & \mathbb{R}^N \\
 \mathcal{W} \downarrow & & \swarrow K \\
 \mathbb{R}^M & &
 \end{array}$$

(a) Relationship between  $\mathcal{A}$  and  $A$  (b) Relationship between  $\mathcal{K}$  and  $K$

$$\begin{array}{ccc}
 \tilde{\mathcal{H}} & \xrightarrow{\mathcal{B}} & \widehat{\mathcal{H}} \\
 \mathcal{W} \downarrow & & \uparrow \mathcal{W}^{-1} \\
 \mathbb{R}^{\ell'} & \xrightarrow{B} & \mathbb{R}^M
 \end{array}$$

(c) Relationship between  $\mathcal{B}$  and  $B$

Figure 6: Commutative diagrams between primal and dual spaces

---

**Algorithm 1** Measurement Map  $\tilde{K}$ 

---

**Input:**  $\hat{A} \in \mathbb{R}^{M \times M}$

Compute Rational Canonical Form, s.t.  $C = Q^{-1}\hat{A}^TQ$ . Set  $C_0 := C$ , and  $M_0 := M$ .

**for**  $i = 1$  **to**  $\ell$  **do**

    Obtain MP  $\alpha_i(\lambda)$  of  $C_{i-1}$ . This returns associated indices  $\mathcal{J}^{(i)} \subset \{1, 2, \dots, M_{i-1}\}$ .

    Construct vector  $v_i \in \mathbb{R}^M$  such that  $\xi_{v_i}(\lambda) = \alpha_i(\lambda)$ .

    Use indices  $\{1, 2, \dots, M_{i-1}\} \setminus \mathcal{J}^{(i)}$  to select matrix  $C_i$ . Set  $M_i := |\{1, 2, \dots, M_{i-1}\} \setminus \mathcal{J}^{(i)}|$

**end for**

Compute  $\mathring{K} = [v_1^T, v_2^T, \dots, v_\ell^T]^T$

**Output:**  $\tilde{K} = \mathring{K}Q^{-1}$

---

---

**Algorithm 2** Sampling locations set  $\mathcal{X}$ 

---

**Input:**  $\widehat{A} = C$ , lower bound  $\ell$

Decompose  $C$  to generate invariant subspaces  $\widehat{\mathcal{H}}_j$ ,  $j \in \{1, 2, \dots, \ell\}$  (see section )

**for**  $j = 1$  **to**  $\ell$  **do**

    Obtain centers  $\mathcal{C}^{(j)}$  w.r.t subspace  $\widehat{\mathcal{H}}_j$ ,

    Generate samples  $x_i^{(j)}$  to create a kernel matrix  $K^{(j)}$  that is shaded only with respect to centers  $\mathcal{C}^{(j)}$

**end for**

**Output:** Sampling locations set  $\mathcal{X} = \{x^{(1)}, x^{(2)} \dots, x^{(\ell)}\}$ .

---

---

**Algorithm 3** Kernel Observer (Transition Learning)

---

**Input:** Kernel  $k$ , basis centers  $\mathcal{C}$ , final time step  $T$ .

**while**  $\tau \leq T$  **do**

- 1) Sample data  $\{y_\tau^i\}_{i=1}^M$  from  $f_\tau$ .
- 2) Estimate  $\hat{w}_\tau$  via standard kernel inference procedure.
- 3) Store weights  $\hat{w}_\tau$  in matrix  $\mathcal{W} \in \mathbb{R}^{M \times T}$ .

**end while**

To infer  $\hat{A}$ , define matrix  $\Phi = \mathcal{W}^T \mathcal{W}$ . Then:

**for**  $i = 1$  **to**  $M$  **do**

At step  $i$ , solve system

$$\hat{A}^{(i)} = ((\Phi + \lambda I)^{-1} (\mathcal{W}^T \mathcal{W}^{(i)}))^T, \quad (11)$$

where  $\hat{A}^{(i)}$ , and  $\mathcal{W}^{(i)}$  are the  $i$ th columns of  $\hat{A}$  and  $\mathcal{W}^{(i)}$  respectively.

**end for**

Compute the covariance matrix  $\hat{B}$  of the observed weights  $\mathcal{W}$ .

**Output:** estimated transition matrix  $\hat{A}$ , predictive covariance matrix  $\hat{B}$ .

---

---

**Algorithm 4** Kernel Observer (Monitoring and Prediction)

---

**Input:** Kernel  $k$ , basis centers  $\mathcal{C}$ , estimated system matrix  $\hat{A}$ , estimated covariance matrix  $\hat{B}$ .  
**Compute Observation Matrix:** Compute the cyclic index  $\ell$  of  $\hat{A}$ , and compute  $K$ .  
**Initialize Observer:** Use  $\hat{A}$ ,  $\hat{B}$ , and  $K$  to initialize a state-observer (e.g. Kalman filter (KF)) on  $\hat{\mathcal{H}}$ .  
**while** measurements available **do**  
    1) Sample data  $\{y_\tau^i\}_{i=1}^N$  from  $f_\tau$ .  
    2) Propagate KF estimate  $\hat{w}_\tau$  forward to time  $\tau + 1$ , correct using measurement feedback with  $\{y_{\tau+1}^i\}_{i=1}^N$ .  
    3) Output predicted function  $\hat{f}_{\tau+1}$  of KF.  
**end while**

---

---

**Algorithm 5** Kernel Controller

---

**Input:** Kernel  $k$ , basis points  $\mathcal{C}$ , estimated system matrix  $\hat{A}$ , estimated covariance matrix  $\hat{B}$ , and function  $f_{\text{ref}}$  to drive initial function to.

**Initialize Observer:** (see Algorithm 4).

**Initialize Controller:** Use Jordan decomposition of  $\hat{A}$  to obtain no. of control locations  $\mathcal{D}$ , compute kernel matrix  $K_{CD} \in \mathbb{R}^{\ell \times M}$  between  $\mathcal{D}$  and  $\mathcal{C}$ , and initialize controller (e.g. LQR) utilizing  $(\hat{A}, \hat{B})$ .

**while** measurements available **do**

- 1) Sample data  $\{y_k^i\}_{i=1}^N$  from  $f(x, \tau)$ .
- 2) Utilize observer to estimate  $\hat{w}_{\tau+1}$ .
- 3) Use  $\hat{w}_{\tau+1}$  and  $f_{\text{ref}}$  as input to controller to get feedback.

**end while**

---

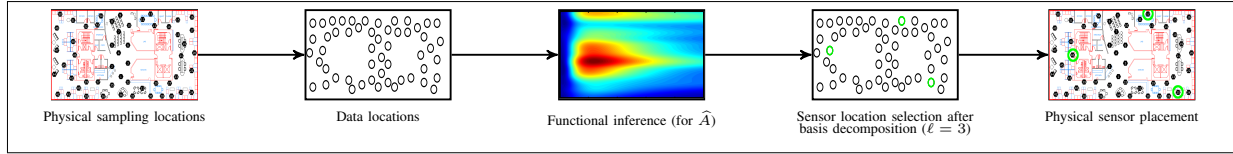


Figure 7: Overall description of how the kernel observer fits in the sensing framework. Physical locations are mapped to data locations, over which historical data is collected as a time series. Functional inference is performed over  $\hat{\mathcal{H}}$  to solve for  $\hat{A}$ . The measurement operator  $K$  is then computed (see Figure 8), leading to sensor placement.

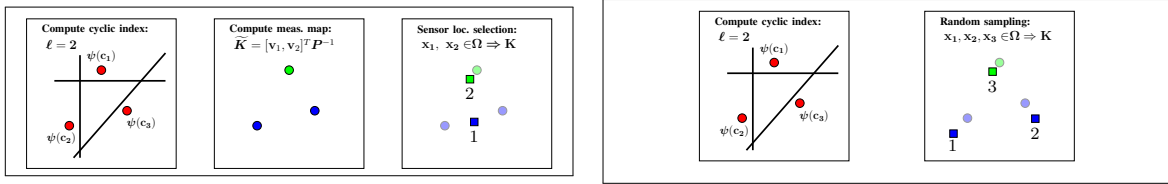
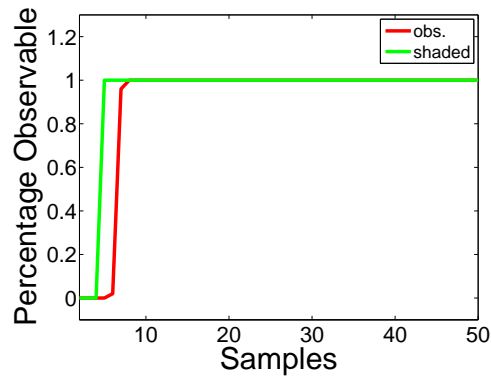
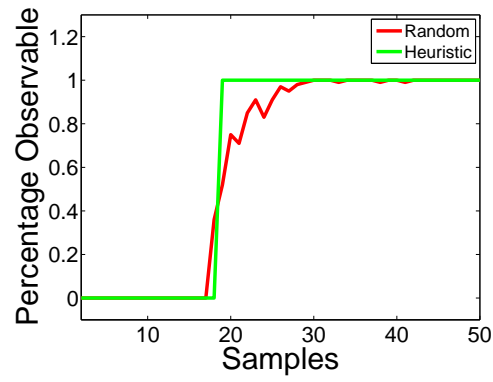


Figure 8: Diagram demonstrating sensor placement using the measurement map or random sampling approaches. The circles represent data locations associated to bases (e.g.  $c_j \Leftrightarrow \psi(c_j)$ ) and the squares represent sensor locations (e.g.  $x_i \Leftrightarrow \psi(x_i)$ ). The cyclic index ( $\ell = 2$ ) indicates how many possible couplings of bases exist, which can be represented as a choice of  $\binom{M}{\ell}$  hyperplanes in  $\Omega$ . If the measurement map is computed (left), the correct couplings are chosen (green vs. blue), and a smaller number of sensors (2) can be placed. Alternatively, random sampling (right) is more computationally efficient, but generally requires more sensors (3).



(a) Shaded vs. observability



(b) Heuristic vs. random

Figure 9: Kernel observability results.

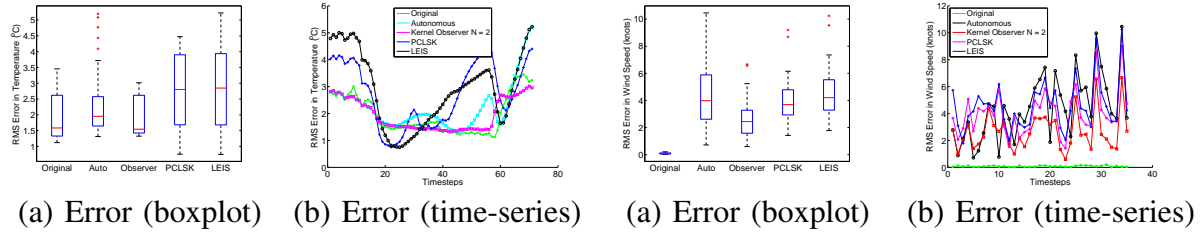


Figure 10: Comparison of kernel observer to PCLSK and LEIS methods on Intel Berkeley dataset.

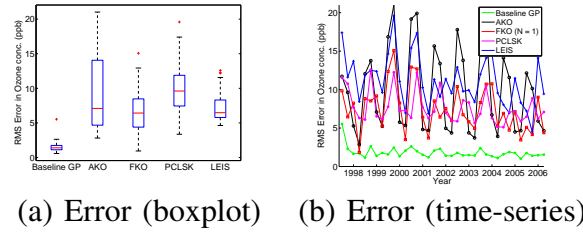


Figure 11: Comparison of kernel observer to PCLSK and LEIS methods on Irish Wind dataset.

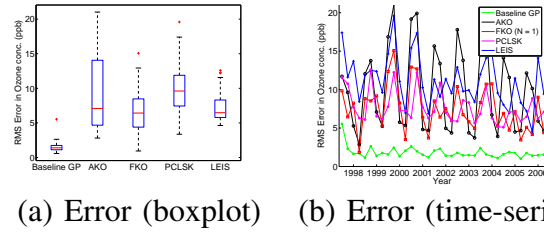
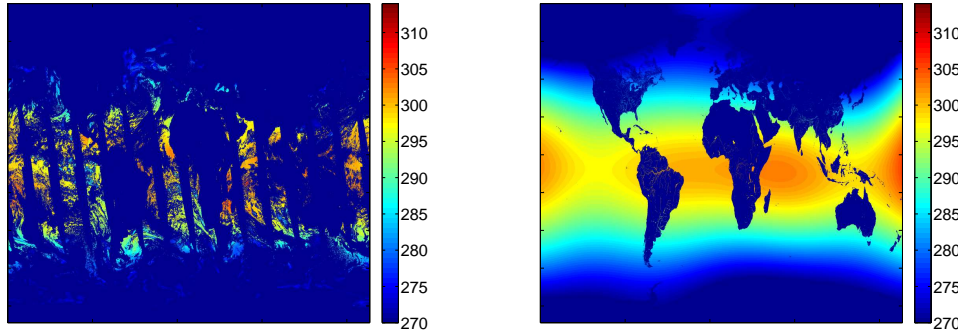
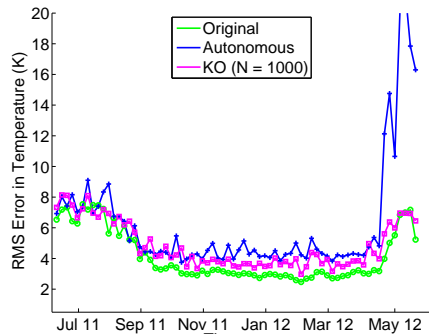


Figure 12: Comparison of kernel observer to PCLSK and LEIS methods on Irish Wind dataset.

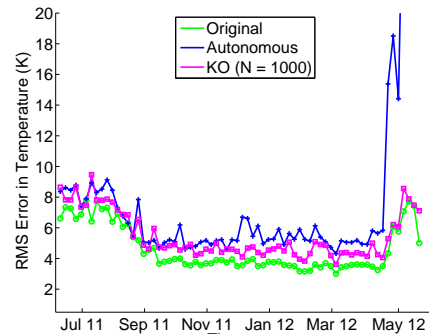


(a) Raw Satellite Data

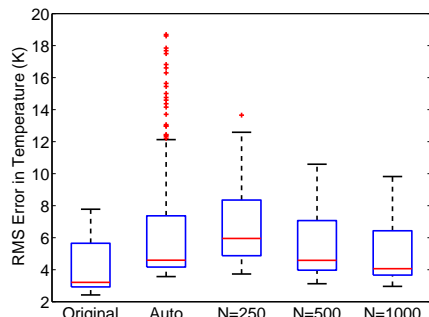
(b) AKO estimate



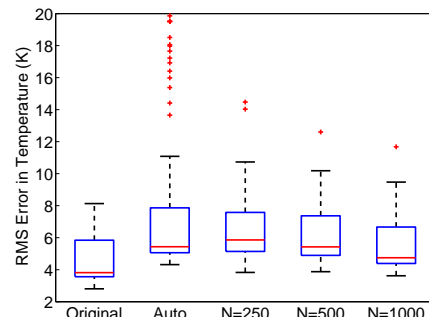
(c) Error-day (time-series)



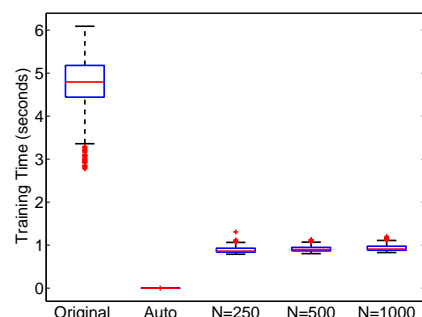
(d) Error-night (time-series)



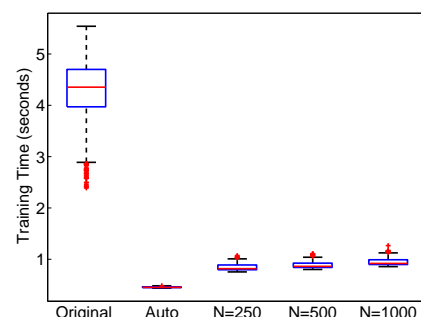
(e) Error-day (box-plot)



(f) Error-night (box-plot)



(g) Estimation time (day)



(h) Estimation time (night)

Figure 13: Performance of the kernel observer over AVVHR satellite 2012 data with different numbers of observation locations.

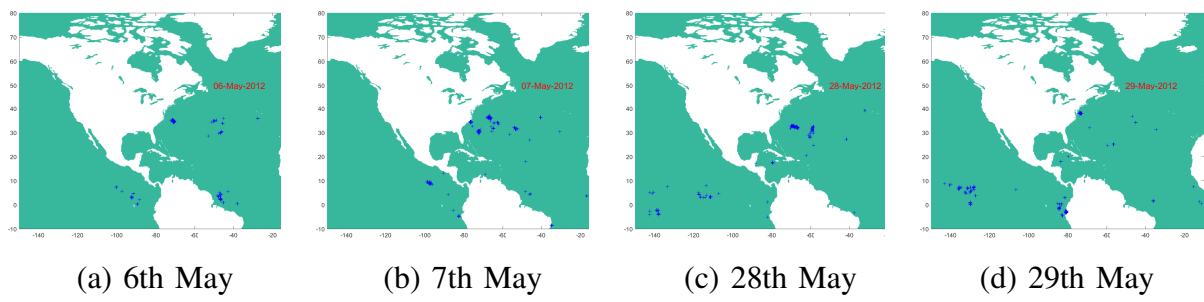


Figure 14: Locations of weather anomaly obtained based on the error between the acutual temperature and the prediction of autonomous kernel observer. Landmass is shown in white and the ocean is in green. Locations marked have error greater than two standard deviations above the mean error.

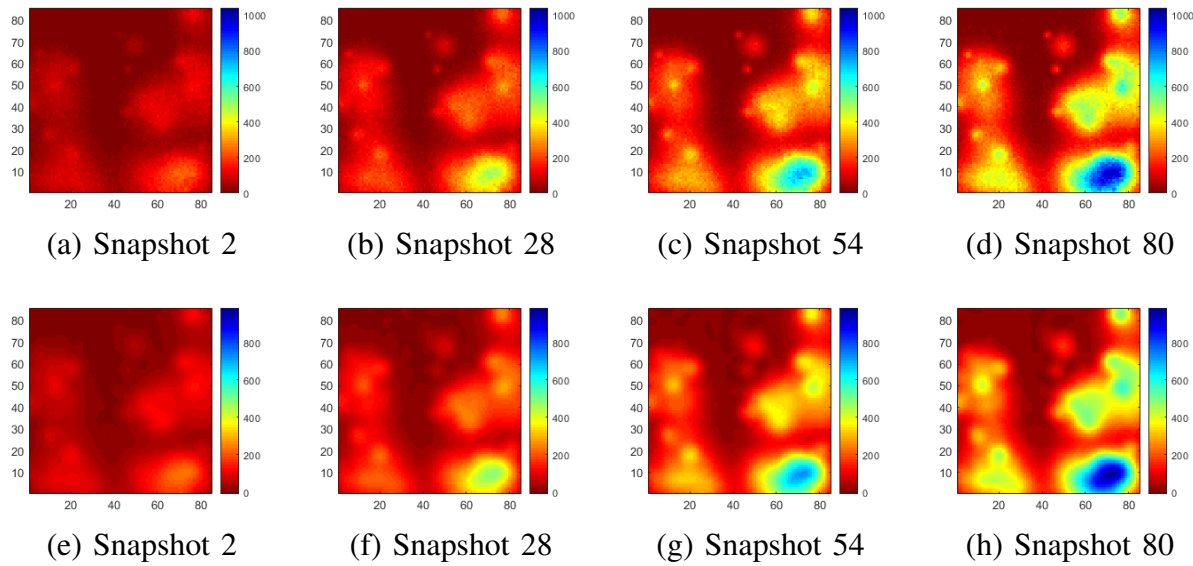
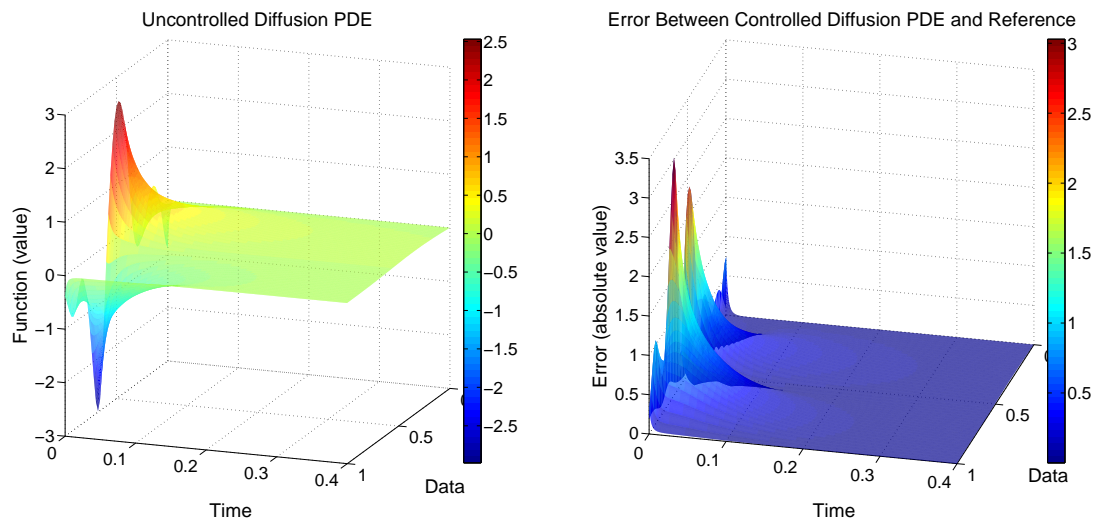


Figure 15: Visualization of Weed Density Growth over 20 days, original (a-d), E-GP (e-h)



(a) Evolution of initial function  $f_{\text{init}}$  according to diffusion equation.  
(b) Error in absolute value between controlled pde and  $f_{\text{ref.}}$ .

Figure 16: Demonstration of the control of a linear diffusion equation.

## Sidebar: Key control problems in agriculture

Shortage of qualified human labor is a key challenge facing farmers [49], [50], leading to smaller profit margins, and preventing the adoption of truly sustainable agricultural practices. Lack of timely available labor was a principle reason behind the tens of millions of dollars of unharvested fruits and vegetables that rotted in California farms in 2017 [51], [52]. Labor shortage can be a major barrier to more sustainable agricultural practices that are more labor intensive.

Many US agricultural systems (particularly in the Midwest) are dominated by annual row crops such as corn and soybean. In the face of labor shortage, this type of agriculture is made practical with heavy reliance on fertilizers, pesticides, and herbicides, applied over large areas with large equipment. Indeed, in row-crops such as corn and soybean, large industrial-scale agriculture is a success story in the United States. In Iowa, for every dollar spent on labor, corn farmers receive \$15-\$20 in income [53]. This highly efficient labor-to-income ratio exists primarily because of the engineering of large agricultural machines that make it practical to seed, spray, and harvest large fields quickly. For example, a 80' tractor can cover 40 acres an hour driving 6 miles per hour. In combination with highly effective seeds, fertilizers, pesticides, and herbicides, large machines have made large scale monocultures for row-crops like corn, soybean, wheat, barley, and sorghum practical and profitable. However, for these crops, lack of timely and actionable information can lead to potentially excessive use of chemicals and energy despite their known large negative environmental impact [54]–[56]. Indeed, excessive use of herbicides coupled with planting of resistant cultivars is a primary reason behind the proliferation of herbicide-resistant weeds in corn and soybean crops in the Midwest [57]–[59], while excessive use of nitrogen, herbicides, and insecticides is linked with the potential harm of chemical runoff into US waterways.

More sustainable alternatives that would not need large amounts of chemicals and other inputs, such as perennial polycultures (mixed species of fruit- and nut-producing trees and shrubs [60], see Figure S2), are currently impractical at scale with current agricultural equipment. Polyculture systems can leverage co-habitation of mutually beneficial plants (and animals, insects, or microbiomes) to create a more sustainable engineered ecosystem. Labor shortage has become a primary barrier to adoption of this sustainable agricultural alternative [61], [62].

One way to address the challenges of labor shortage in agriculture is by enabling a tightly integrated chain of information-driven technologies that automate the entire production chain in agriculture, from seed breeding and chemical production, to farming, and trade of agricultural products. Such an integrated *digitalfarm of the future* can be enabled if data from multiple

modalities and platforms is integrated together to inform **decisions** which can then be transformed into management**actions** on the farm with automated equipment. Indeed, there are many ongoing independent efforts to enable the farm of the future: Large equipment companies are automating their equipment and enabling new levels of precision; startups are accelerating the proliferation of 5 small equipment such as drones and small robots for monitoring and management on farms, and data integration and interpretation companies are changing the way growers process, consume, and interact with data.

Here we outline some of the fundamental challenges in autonomy, estimation, and control that the controls community can help overcome to enable the digital farms of the future:

10        **Persistent multi-agent autonomy under partial observability:** The digital farm of the future will employ teams of distributed heterogeneous agents to autonomously manage, optimize, and harvest large acres of diverse crops across the entire season without encumbering humans. This level of autonomy in unstructured field environments is out of reach of the current state-of-the-art which requires constant human monitoring and oversight, especially in the presence 15 of change or unforeseen events. Efficient and reliable control will be central to the success of these robots. Small below-canopy robots (e.g. Figure S1 [63]) will need to provide precision care including pruning, weeding, and re-seeding without damaging plants or causing soil compaction. Deployed at scale, these robots can not only make large scale organic farming practical, but also enable enhanced breeding through field-scale phenotyping [63]–[65]. *The big controls challenge* 20 *here is in making decisions over large spatiotemporal scales with information obtained from a few stationary and mobile sensors which can only partially observe the environment at any given time.* The strong theoretical underpinnings in the controls community on autonomy, distributed and networked systems, and estimation can be of tremendous value in engineering digital farm systems consisting of distributed teams of autonomous agricultural robots.

25        **Dexterous and ubiquitous robotics for precise care:** The digital farm of the future will strive to eliminate costly inputs (chemicals, labor, energy, and knowledge) with low-cost, dexterous, and highly autonomous agricultural equipment [66]. Advances in *soft* arms and grippers can enable robots that can have far better reach and dexterity around plants than robots equipped with traditional *hard* industrial robotic arms. Soft arms, which are often actuated with 30 pressurized tubes, can be far less expensive to manufacture and significantly lighter than their hard counterparts. On the other hand, soft arms can be slow to actuate and have limited payloads. To make soft robots practical, optimal feedback control techniques are necessary that work with conformal objects with very large degrees of freedom. In particular, soft arms tend to significantly deform under weight and behave quite differently when loaded with different payloads. Unlike 35 hard arms, encoders are not sufficient to estimate the pose of the arm or the manipulator. Strain

and angle sensors need to be positioned judiciously to keep costs down, and image based feedback control will be necessary.

**Control of complex designed ecosystems:** Agricultural ecosystems designed with synergistic biodiversity – known as *polycultures* – have long been proposed as alternatives to traditional monoculture-based agriculture [67]–[70]. Based on studies of a range of natural ecosystems, polycultures are expected to be sustainable, productive, resilient and ecologically beneficial, requiring far less chemical inputs for food production. However, compared to their widely practiced counterparts (traditional monocultures such as corn and soybean), polyculture production systems have not yet been demonstrated to be profitable at large scale. This is primarily due to their labor- and knowledge-intensiveness, stemming from their inherent complexity. Indeed, despite their clear benefits and the potential to be profitable, optimizing and managing such complex systems can be difficult, even for those with training and experience in polycultures.

The complex interaction between closely-spaced diverse plant species in a polyculture results in both spatial and temporal dynamics as the plants grow and interact with each other. Plant growth often exhibits hybrid dynamical systems behavior with rapid thresholded growth bursts followed by slow progression. The triggers for growth bursts are dependent on environmental factors such as temperature, soil moisture, and sunlight reaching individual and cumulative thresholds, and complex interrelations between neighboring plants, soil chemistry, insects, and soil microbes. Simulating individual plant growth is an active area of research with many open questions in modeling and plant biology [71]. Arguably, very high resolution plant growth models may not even be necessary for effective control of polycultures. Yet on the other hand, the existing models of plants and interactions with ecosystems [72]–[77] are not well suited for designing and managing polycultures because of the simplifying assumptions that are often made. A good balance could be struck with data driven machine learning models that have sufficient resolution for aggregate prediction over multiple spatiotemporal scales and are lightweight enough for control and decision making. With these models, predictive control strategies can be created that task teams of robots for management tasks. Furthermore, these predictive models can enable quantified mechanisms of design and planning of efficient agroecosystems. Obtaining the required data to train these models and using them to create effective control techniques for managing profitable polycultures remains an exciting direction of future work where the control community can help.

The discussion in this sidebar was informed by many conversations with crop scientists at UIUC. In particular, *the authors wish to thank Prof. Stephen Long and Prof. Carl Bernacchi for insights on the phenotyping bottleneck and simulation of plants (crops-in-silico), Prof. Adam*

*Davis on inputs on the herbicide resistant weed crisis, and Prof. Sarah Lovell on sustainable agricultural production systems and perennial polycultures, as well as the members of the UIUC Center for Digital Agriculture*

## Sidebar: Feature Spaces in Machine Learning

Suppose we have data  $\mathcal{D} = \{(x_1, y_1), \dots, (x_N, y_N)\}$ , where  $x_i \in \Omega_I$  and  $y_i \in \Omega_O$ . Here,  $\Omega_I$  is the input domain, and is generally a subset of  $\mathbb{R}^D$ , although more general sets such as discrete spaces, graphs, or text documents can be considered. Similarly,  $\Omega_O$ , the output domain, can be just as general as  $\Omega_I$ . We wish to solve for functions  $f$  in some space of functions  $\mathcal{J}$  such that  $f(x_i) = y_i \forall i$ . Generally, to restrict the complexity of the space  $\mathcal{J}$ , a *loss function*  $L(f, \mathcal{D}) \mapsto \mathbb{R}$  is chosen, which measures the error between a prediction  $f(x_i)$  given a datapoint  $x_i$ , and  $y_i$ , averaged over the entire dataset  $\mathcal{D}$ , and the optimization problem becomes

$$f^* = \arg \min_{\mathcal{J}} L(f, \mathcal{D}) + \lambda g(f), \quad (\text{S1})$$

where  $\lambda \in \mathbb{R}$ , and  $g(f)$  represent some constraints on the function  $f$ , such as smoothness. Control theorists are most likely familiar with input-output pairs where  $x_i \in \mathbb{R}^N$  and  $y_i$  is either in  $\mathbb{R}$  or  $\mathbb{R}^M$  (*regression*). In machine learning, the most common task is when the  $y_i$   
5 are discrete (*classification*). Different combinations of task, loss functions, and spaces  $\mathcal{J}$  result in different algorithms to solve these problems, which can sometimes form entire subfields of machine learning.

The choice of the function space  $\mathcal{J}$  can be critical for the task we want to perform, similar to how the choice of the state space is in control theory. Let's consider a simple example. Suppose we have data from two *classes*  $\mathcal{D}_A = \{(x_1^A, y_1^A), \dots, (x_N^A, y_N^A)\}$  and  $\mathcal{D}_B = \{(x_1^B, y_1^B), \dots, (x_N^B, y_N^B)\}$ , where  $x_i^{\{A,B\}} \in \mathbb{R}^D$ , and  $y_i^{\{A,B\}} \in \{-1, +1\}$ , shown in Figure S3a. Let  $f$  be chosen from the class of linear algorithms, i.e.  $f = w^T x + b$ , where  $w \in \mathbb{R}^D, b \in \mathbb{R}$ . We pick a loss  $L$  that returns a loss of zero when the prediction is the correct class, and if the prediction is the incorrect class, returns a higher value for misclassifications that are closer to the boundary. A classical example of such a loss is that used by the *perceptron algorithm*, which can be written as

$$L(f, \mathcal{D}) = \frac{1}{N} \sum_{i=1}^N \max(0, -y_i w^T x). \quad (\text{S2})$$

This loss measures how accurate the prediction of the perceptron is on average. The general algorithm is as follows:

- 10 1) Initialize  $w \in \mathbb{R}^D$  to all zeros.
- 2) For a fixed number of iterations, or until some stopping criterion is met:
  - a) For each training example  $(x_i, y_i)$ ,
    - i) Let  $\hat{y}_i = \text{sgn}(w^T x_i)$ .
    - ii) If  $y_i \neq \hat{y}_i$ , update  $w \leftarrow w + y_i x_i$ .

The perceptron was one of the first machine learning models, and the genesis of modern neural networks [78]. Figure S3 shows a visual representation of where the perceptron algorithm can solve for the decision boundary with zero error. However, if the structure of the data has some nonlinearities, no solution will be found, as seen in Figure S4. In this case, the original space 5 the data resides in is, in some sense, not a rich enough representation. If we could construct a mapping of the data to a different space which gives a learning algorithm more degrees of freedom to work with, linear algorithms can still be deployed. If we map the same data using a nonlinear map  $\phi(x, y) := (x^2, y^2, 2xy)$ , the perceptron now finds a solution in 3 dimensions, as seen in Figure S5. This example shows why so much of the work in machine learning focuses on 10 learning the right representation for the data, for the right representation makes the classification task easy. Two major threads of research in the arena of feature maps over the last 40 years are kernel methods, and neural networks, the latter of which has gained remarkable notoriety in the last 10 years. These lines of research represent distinctly different strategies for generating feature maps from data.

In Figure S4, the data was mapped using an explicit feature map. Kernel methods, of which Gaussian Processes are a great example, utilize an elegant strategy for generating feature maps from data, using a remarkably simple trick called *the kernel trick*. Given a positive-definite kernel function  $k(x, y) : \Omega \times \Omega \rightarrow \mathbb{R}$ , Mercer's theorem guarantees the existence of a feature map  $\psi : \Omega \rightarrow \mathcal{H}$ , where  $\mathcal{H}$  is a *reproducing kernel Hilbert space (RKHS)*, and the map  $\psi$  obeys the property

$$k(x, y) = \langle \psi(x), \psi(y) \rangle_{\mathcal{H}}. \quad (\text{S3})$$

15 Recall that since  $\mathcal{H}$  is an RKHS, given  $c \in \Omega$ ,  $k(x, c) = \langle \psi(x), \psi(c) \rangle_{\mathcal{H}}$ , and  $k(x, c) := \psi_c \in \mathcal{H}$ . Furthermore,  $\text{span}\{\psi_x\}_{x \in \Omega}$  is dense in  $\mathcal{H}$ . There exist kernels that generate  $\mathcal{H}$ s that are extremely high dimensional: for example, the RBF kernel  $k(x, y) = e^{-\gamma \|x-y\|^2}$  is infinite-dimensional. This high degree of freedom enables the design of powerful learning algorithms that are linear in  $\mathcal{H}$ , but nonlinear in the input domain  $\Omega$ . The canonical example of this is the support vector 20 machine (SVM) [79], but a more instructive example for us is the perceptron algorithm.

Suppose we trained a perceptron using  $\mathcal{X} = \{x_1, \dots, x_N\}$ ,  $x_i \in \mathbb{R}^D$  for some  $D$ ,  $y_i \in \{-1, 1\}$ . The prediction of the perceptron is  $\hat{y} = \text{sgn}(w^T x)$ , where  $w \in \mathbb{R}^D$ . It can be shown that  $w = \sum_{i=1}^n \alpha_i y_i x_i$ , where  $\alpha_i$  is the number of times  $x_i$  was misclassified. This allows us to derive the dual version of this algorithm, because

$$\hat{y} = \text{sgn}(w^T x) = \text{sgn} \sum_{i=1}^n \alpha_i y_i \langle x_i, x \rangle_{\mathbb{R}^D}.$$

The dot product  $\langle x_i, x \rangle_{\mathbb{R}^D}$  can be replaced with the kernel, leading to the *kernel perceptron algorithm*:

- 1) Initialize  $\alpha \in \mathbb{R}^N$  to all zeros.
  - 2) For a fixed number of iterations, or until some stopping criterion is met:
    - a) For each training example  $(x_j, y_j)$ ,
    - i) Let  $\hat{y}_j = \text{sgn} \sum_{i=1}^n \alpha_i y_i k(x_i, x_j)$ .
    - ii) If  $y_j \neq \hat{y}_j$ , update  $\alpha_j \leftarrow \alpha_j + 1$ .
- 5

This algorithm is nonlinear in the input domain, but linear in the feature space  $\mathcal{H}$ , which led the deep learning community to, somewhat pejoratively, label this as an example of a *shallow learning architecture*. Kernel methods can also be used in a more direct fashion: if we have a subspace  $\mathcal{H}' \subset \mathcal{H}$  with a basis generated from  $\mathcal{C} = \{c_1, \dots, c_M\}$ , i.e.

10

$\mathcal{H}' = \text{span}\{\psi_{c_1}, \dots, \psi(c_M)\}$ , a linear model in  $\mathcal{H}'$  is again given by a vector  $w \in \mathbb{R}^M$ . Suppose this weight vector represents a boundary in  $\mathcal{H}'$ : to compute which side of this boundary a point  $x$  would lie on in  $\mathcal{H}'$ , we simply compute  $\text{sgn}(\sum_{i=1}^M w_i \langle \psi(x), \psi(c_i) \rangle_{\mathcal{H}}) = \text{sgn}(\sum_{i=1}^M w_i k(x, c_i))$ . The choice of the kernel and its parameters depends on the dataset and the loss function.

15

The kernel and the data together form the feature space. Because kernel methods are linear in their parameters and are restricted to RKHSs, they are amenable to somewhat straightforward mathematical analysis, and are very well studied because of this. We refer the reader to the very recent review of Gaussian processes in control that appeared in IEEE CSM for further examples and software relating to GPs and their use in control [16]. We switch our attention now to a different way of obtaining the features: Deep Neural Networks. While GPs build features using

20

positive semidefinite symmetric kernels that compare any two points, DNNs build features using nested nonlinear operations.

Deep neural networks (DNNs) are models where the representing function  $f$  has nested nonlinearities. Fix a width  $M \in \mathbb{N}$ . Deep nets are parameterized models with weight matrices  $W^l \in \mathbb{R}^{M \times M}$ , bias vectors  $b^l \in \mathbb{R}^M$ , and a pointwise nonlinearity  $\phi : \mathbb{R} \rightarrow \mathbb{R}$ , with  $l = 1, \dots, L$ . Vectors  $h^l \in \mathbb{R}^M$  are called preactivations, and  $x^l \in \mathbb{R}^M$  are called postactivations, each element of which is called a *neuron*. Let  $h^0 \in \mathbb{R}^M$  be the input: then the canonical feedforward neural network is given by

$$x^l = \phi(h^l), \quad h^l = W^l x^{l-1} + b^l. \quad (\text{S4})$$

Therefore, we have that  $f(h^0) = x^L$ . The individual steps  $l$  are called the *layers* of the network, and the nesting property allows these networks to learn much more complicated functions than shallow architectures given the same number of nonlinearities [80]. Different choices of

25

nonlinearities, connections, and layer architectures lead to different types of neural networks, which are used for different applications [81]. Deep learning has had an enormous impact on both the machine learning literature and industrial applications, and that impact has bled over rapidly to other fields. Due to the nested structure of nonlinearities in DNNs, they are more difficult to analyze using simple mathematical tools, and therefore most of the literature in

30

the field has focused on the empirical performance of these methods, where they significantly

outperform competing methods. The significance of the achievements of machine learning in general and deep learning in particular have been in its ability to simplify the implementation of complex functional representation, essentially, in its ability to make system identification more accessible for difficult problems. However, the feature spaces generated by deep networks  
5 are not as well behaved and accessible to analysis as those generated by kernel models. In particular, deep network feature spaces do not naturally have the properties of RKHSs. This presents one barrier to analyzing and understanding the nature of these models. For the reliable and verifiable inclusion of DNNs in engineering control systems, further insights are necessary into the structure of the feature spaces these models generate, to restrict certain forms of output,  
10 and to shape decision-making.



Figure S1: The TerraSentia robots developed by Chowdhary's group at UIUC and commercialized by EarthSense inc. Agricultural robots such as these present exciting possibilities for distributed agricultural management with teams of compact, ultra-light, under-canopy robots equipped with advanced autonomy and machine learning. Such robots can fill the niche between large farm equipment and manual labor, as well as enable perennial polycultures, and closer to home, they could also weed your garden! Advances in persistent multi-agent autonomy in harsh, changing, and uncertain environments driven by the controls community are driving such exciting possibilities of the future of agriculture.

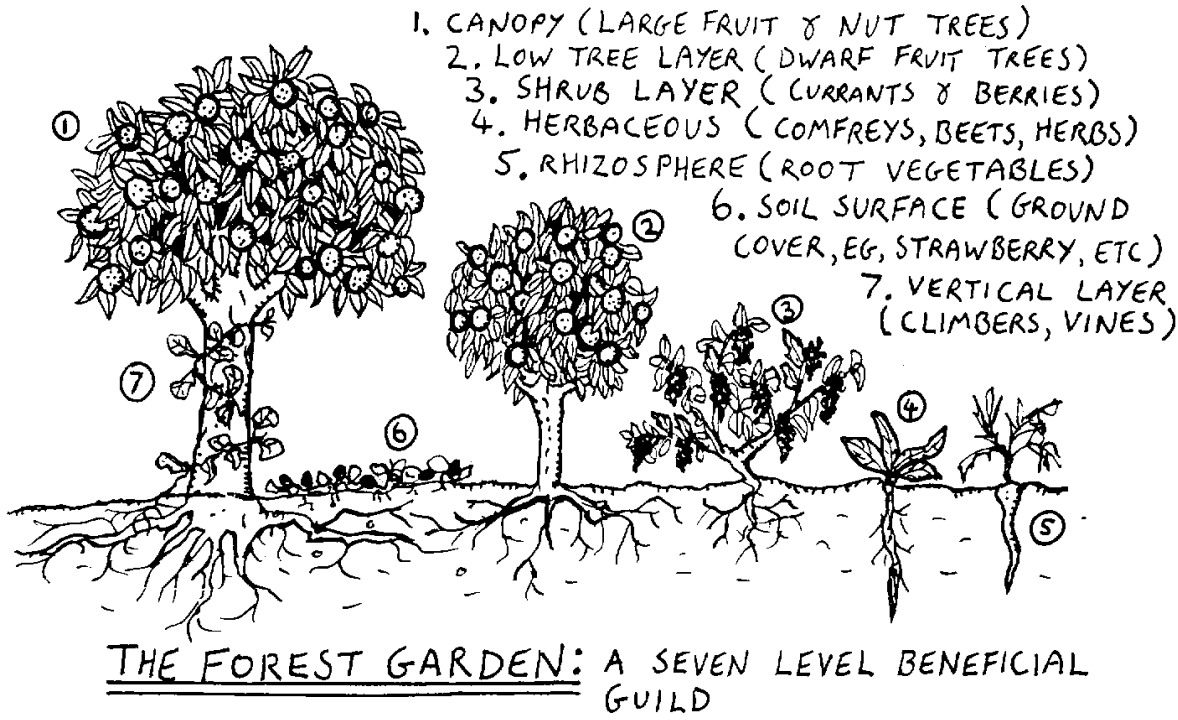


Figure S2: The seven layers of the forest garden. Polyculture agricultural production systems are designed ecosystems that can be more productive and sustainable than traditional monoculture systems. Managing such complex systems requires fundamental advances in robotics, spatiotemporal modeling, and control of complex biological processes, all areas where the control community can help. Figure source [82] see also [83].

## Sidebar: Learning Fluid Flows with Evolving Gaussian Processes

2nd order Partial Differential Equations (PDEs) are ubiquitous in practical science and engineering, from mechanics to transport phenomena to electromagnetics. In our view, the Navier-Stokes equations governing fluid dynamics represent most, if not all of the overall complexity of modeling these as (a) it exhibits of hybrid system behavior, e.g. elliptic-hyperbolic, and (b) the nonlinearity results in the complex spatio-temporal dynamics that are prevalent in many practical situations. The form of the NSE for compressible Newtonian fluids is expressed below, where  $\mathbf{u}$  is the fluid velocity,  $p$  is the fluid pressure,  $\rho$  is the fluid density, and  $\mu$  is the fluid dynamic viscosity. [84]

$$\rho \left( \frac{\partial \mathbf{u}}{\partial t} + \mathbf{u} \cdot \nabla \mathbf{u} \right) = -\nabla p + \nabla \cdot (\mu(\nabla \mathbf{u} + (\nabla \mathbf{u})^T)) + \nabla \left( -\frac{2\mu}{3} \nabla \cdot \mathbf{u} \right) + \rho \mathbf{g}$$

We demonstrate the Evolving Gaussian Processes method on CFD data of flow over a bluff body (a cylinder) over a range of Reynolds numbers from 100 to 1000 (the Reynold number is dimensionless flow rate). This deterministic, high-dimensional spatiotemporal dynamical system is well-studied in the fluid dynamics literature, both experimentally and numerically [85]–[87]. The conventional wisdom would be to learn a separate model over each Reynolds number, but our results show that the E-GP method is capable of learning the dynamics of all the flow patterns at once. Using the learned dynamics over weights of successive kernel models, E-GP is capable of predicting the future states of functional evolution in a recursive manner. The key advantage of E-GP is that evolution of large function spaces can be transformed into learning the evolution of a relatively smaller Hilbert space which is encoded by the kernels and the associated weight vector. Furthermore, the values of the weights and the associated linear dynamical systems provide critical insights, such as spatial-correlations through the structure of the transition matrix, local modes of dynamic evolution through invariant subspaces of the transition matrix, and eigenmodes of evolution. The latter is of significant importance to the ongoing work in Koopman operator models of spatiotemporal phenomena.

In our CFD simulation, we used a 4th-order polynomial expansion with spectral element method on the incompressible Navier-Stokes equation to generate the cylinder flow data for  $Re = 100, 300, 600, 800$ , and  $1000$ . The spatial domain is  $[-2, 10] \times [-3, 3]$ , excluding the diameter-1 cylinder at the origin. Neumann boundary conditions are applied to the far-field of the cylinder in the  $y$ -direction and the outlet of the flow field; and a Dirichlet boundary condition is applied to the inlet. Each data set contains at least 200 snapshots with a uniform time step of  $\tilde{0.03}$  sec. Each snapshot contains 24,000 velocity data points for  $Re=100$  or 95,000 velocity data points for  $Re=300,600,800,1000$ . Each data set took at least 10 hours in a high performance computer

cluster to generate. Figures S6,S7(a-d) visualize the horizontal velocity for Re=100 and Re=1000, with red being the greatest negative velocity and blue the greatest positive velocity. The flow is unstable, periodic, and clearly nonlinear.

We used the Gaussian RBF kernel  $k(x, y) = e^{-\|x-y\|^2/2\sigma^2}$  in our E-GP model, with  $\sigma$  estimated to be 0.4. Using a budget of 600 kernel centers (see Figure S9a-S9b, and note how they cluster in the most dynamic regions), we find a  $600 \times 600$  matrix  $\hat{A}$  which accurately (Figure S8a) captures the dynamics of the nonlinear system. We can use this to propagate single initial condition  $w_0$  forward to make predictions, then compare the predictions to the original training data. We found total percentage errors between 3% for Re=100 and 7-8% for Re=1000, as can be seen in the solid lines in Figure S8a. We define the total percentage errors as  $E_\tau = \frac{\|\bar{y}_\tau - \bar{y}_\tau\|_2}{\|\bar{y}_\tau\|_2}$  where  $\bar{y}_\tau$  is the output vector for time  $\tau$  and  $y_\tau$  is the E-GP estimate at that time. Note that *the size of the model has been reduced by almost two orders of magnitude* from the original CFD data. This process takes about 13 minutes in MATLAB for a 200 snapshot by 95,000 point set on an ordinary Intel i7 4.00 GHz processor.

## **One Transition Matrix for Everything**

In order to approach the challenge of generalizing across similar spatiotemporally evolving systems, the first question we had to answer is whether we can find an  $\hat{A}$  matrix that accurately captures the dynamics of multiple similar flows. The answer to that question is *yes*, using the trajectory concatenation method. Amazingly, a single model generated this way works almost as well on all five data sets as do five individual models trained on each data set separately. This is confirmed by both the total error plots (Figure S8a), which show only slight increases in each of the total percentage error plots, and visual inspection of the dynamic modes displayed. This result is even more surprising in light of the fact that the rate of vortex shedding for each Reynolds number is different. By taking a Fourier transform of the time evolution of a data point located at (0.5,8), we find that for the original data sets the vortex shedding frequency is 0.448 Hz, 1.260 Hz, 1.380 Hz, 1.388, and 1.401 Hz for Re=100, 300, 600, 800, and 1000 respectively, and for the E-GP models the frequencies are 0.452 Hz, 1.21 Hz, 1.36 Hz, 1.36 Hz, and 1.36 Hz respectively.

## **Generalizing from Learned Dynamics to Unknown Dynamics**

Having seen that it is possible to find a single transition in the weight space that models the dynamics systems over a range of parameters, the next challenge is to be able to model flows with parameters that the model has not been trained on. We derived an  $\hat{A}$  matrix from the Re=100, 300, 600, and 1000 data sets and tested it against the Re=800 data set. The results are below in Figure S8b. For the first 120 snapshots, the total percentage error remains under

10%, which is satisfactory. After this, however, the total percentage error curves upwards as the slight errors in the transition matrix compound. Over 800 snapshots, we found an average total percentage error of less than 25%.

## Linear Dynamical Layer Analysis & Insights

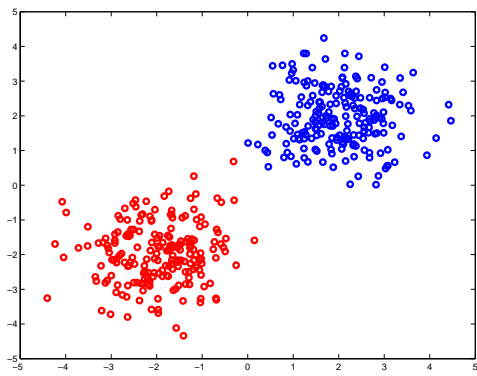
5 Due to the spatial encoding of the weights which the linear transition model operates on, we are able to analyze the dynamics and find physical insights into the process. We demonstrate two techniques: (1) using eigendecomposition of the transition matrix to discover the eigenfunctions and invariant subspaces of system, and (2) visualizing the most significant spatial interactions in the system.

10 An invariant subspace of a linear operator is a subspace of the Hilbert space such that any vector in the subspace remains in the subspace under transformation by the operator. By marking which kernel centers are associated with different subspaces, we can spatially separate the space into multiple dynamic modules. The physical insight is some areas of the space are dynamically entangled with each other, and other are independent of each other. For those  
15 interested in monitoring spatiotemporally evolving systems, the number and location of the invariant subspaces determines how many and where feedback sensors ought to be for robust prediction of the weights. Before doing the Jordan decomposition of  $\hat{A}$ , we zero any elements smaller than some small  $\varepsilon$  in order to stabilize the algorithm for matrices with many elements close to zero. Afterwards we visualize the eigenvector matrix using a *logarithmic* color chart,  
20 as seen in Figures S9a,S9b,S9c. These plots are for models trained individually on Re=100 and Re=1000 with 300 kernels, and on all five with 600 kernels, for comparison. We see three categories of eigenvector in the rows: (1) Rows at the bottom that have exactly one non-zero elements, (2) In the middle, a couple rows with a dozen significant elements, and (3) at the top a number of rows that affect the majority of the kernel centers in the space.

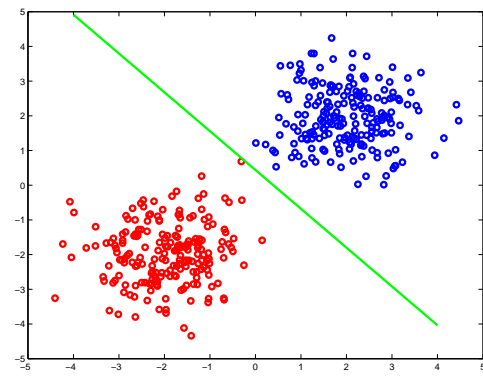
25 Each eigenvector of (1) spans its own invariant subspace, and is depicted in magenta circles in Figure S10. Category (3) is one invariant subspace, depicted with black crosses. Category (2) is subsumed in Category (3). The figures show that the dynamics near/around the cylinder and in its wake are so entangled that a single sensor measurement in that area may be sufficient to estimate over that entire subspace. On the other hand, areas far from the core of dynamic  
30 excitement are their own independent, invariant subspaces, and thus must be monitored locally.

Another way to visualize the operation of the linear transition matrix is to plot lines between kernel centers that are influencing each other strongly. That is, if we draw a line center  $c_j$  to  $c_i$  for each of the (relatively) largest elements  $a_{ij}$  of  $\hat{A}$ , one can see how the system dynamics are coupled spatially (Figures S11a,S11b,S11c). We can also plot the magnitude of  $a_{ij}$  in a third

axis for further insight into the most dominant dynamic connection in the system.



(a) Data from classes  $A$  and  $B$ .



(b) Linear boundary separating data.

Figure S3: Example of linearly separable data. Any simple linear learning algorithm e.g. perceptron, finds a solution.

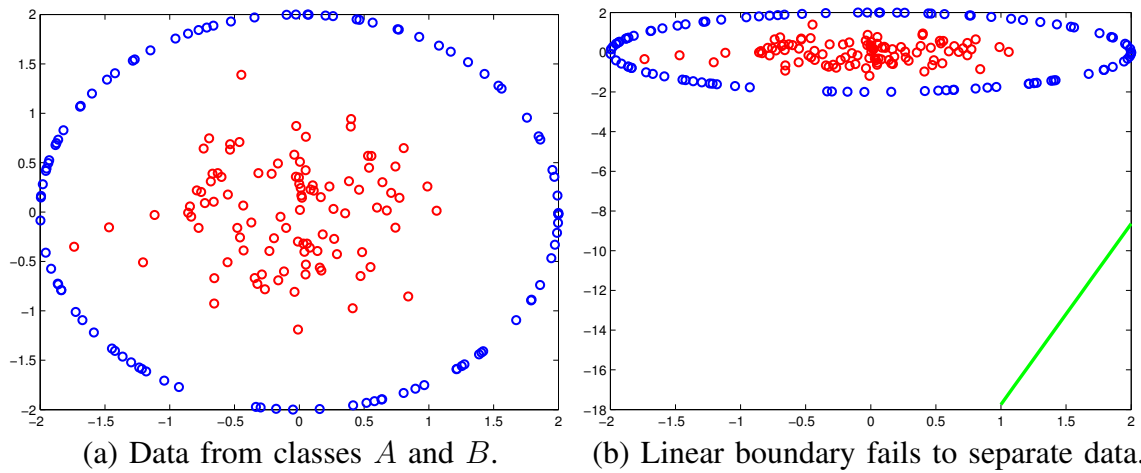
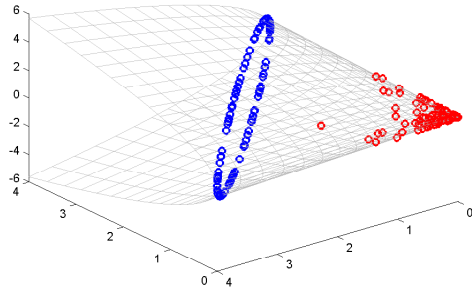
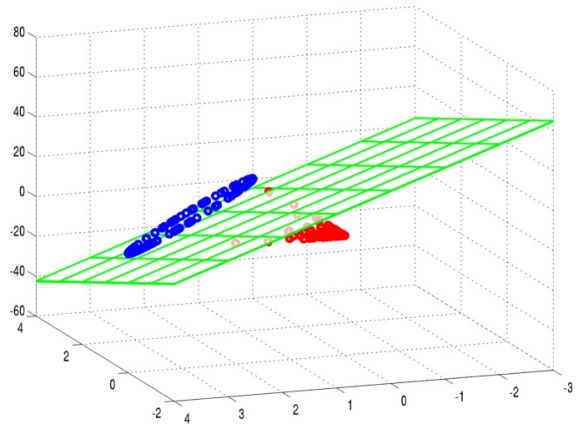


Figure S4: Example of nonlinearly separable data. Perceptron fails to find a solution, and diverges.



(a) Nonlinear mapping of data.



(b) Linear boundary in new space.

Figure S5: If we map the same data using a nonlinear map  $\phi(x, y) := (x^2, y^2, 2xy)$ , the perceptron now finds a solution in 3 dimensions.

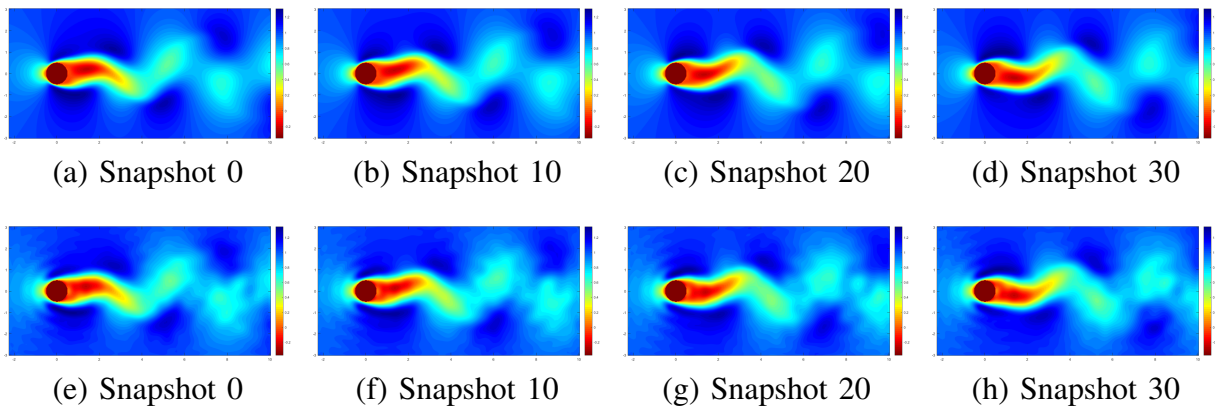


Figure S6: Visualization of Fluid Flow at  $\text{Re} = 100$ , CFD (a-d), E-GP (e-h)

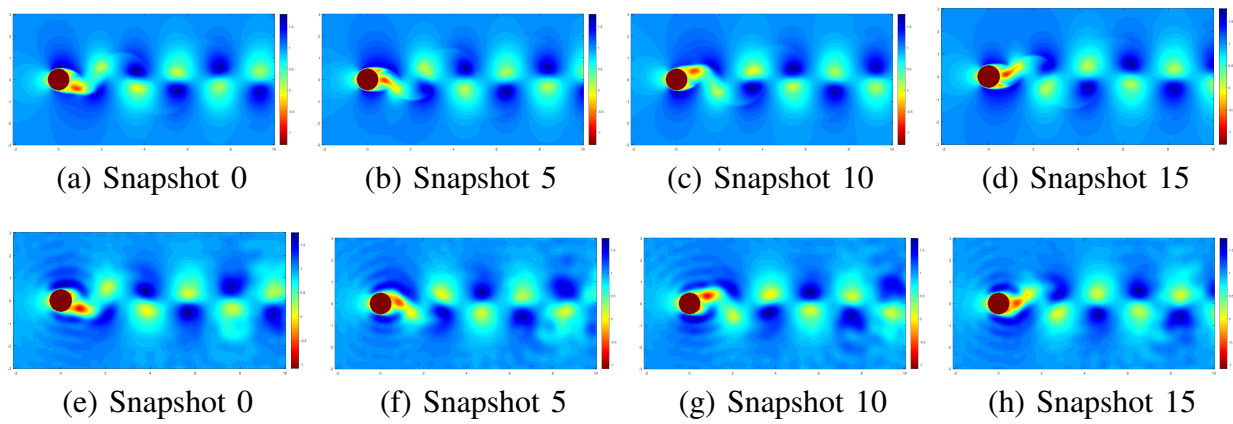


Figure S7: Visualization of Fluid Flow at  $\text{Re} = 1000$ , CFD (a-d), E-GP (e-h)

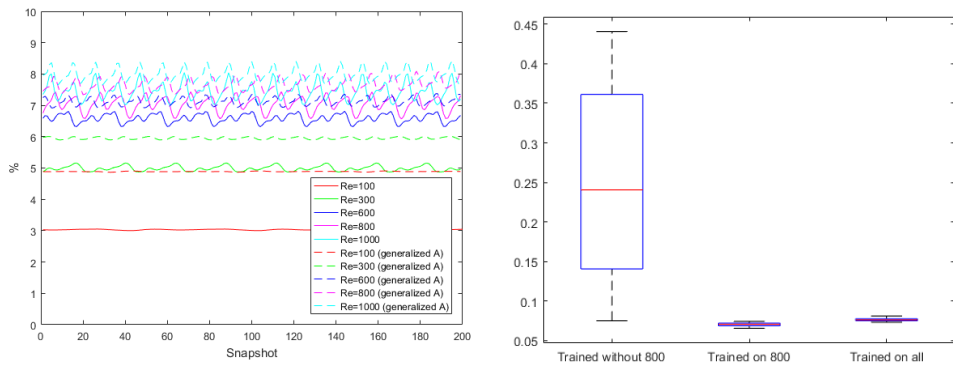
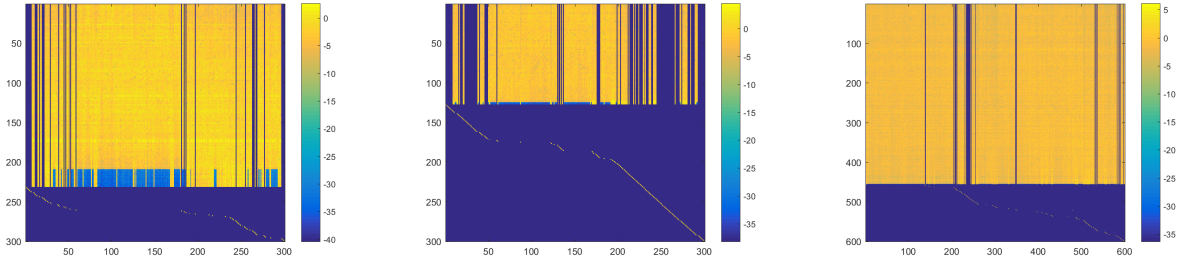


Figure S8: Total Percentage Errors



(a)  $\text{Re} = 100, \varepsilon = 0.005$

(b)  $\text{Re} = 1000, \varepsilon = 0.05$

(c) All Reynolds numbers,  $\varepsilon = 0.069$

Figure S9: Eigenvector Heat Maps

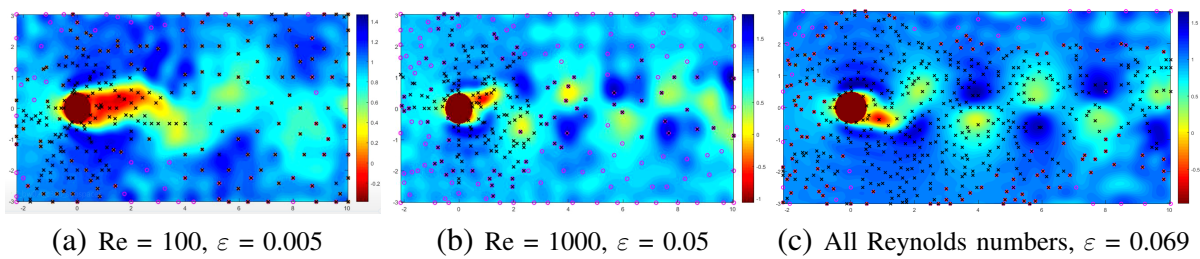


Figure S10: Invariant Subspaces

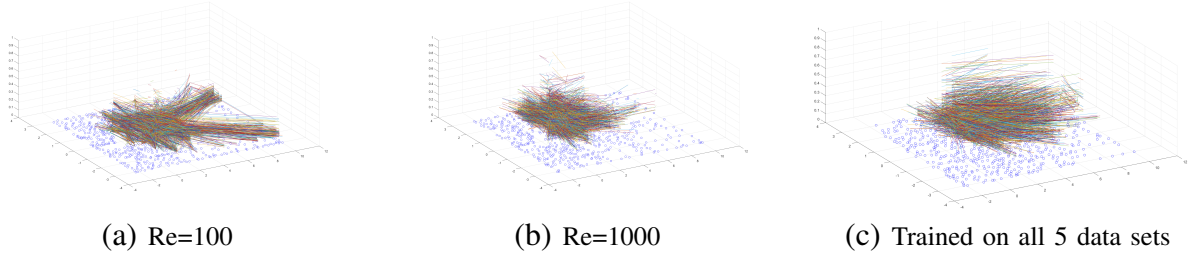


Figure S11: Visualization of Co-Relations in Transition Matrix

## Author Biography

**Harshal Maske** is completed his PhD in 2017 from the University of Illinois in Urbana-Champaign, he is currently a postdoc at UIUC. He received his Masters and Bachelors integrated degree in Mechanical Engineering from the Indian Institute of Technology Kharagpur, India, in 5 2009. After completing his masters, he worked for three years at Defense R&D Organization (2009-2012), India and for one year at John Deere (2012-2013). His current research is grounded in the theory at the intersection of Controls and Machine learning with the aim of developing data driven models with theoretical guarantees that enable decision making and control in real-world, complex problems.

10 **Hassan A. Kingravi** is a senior data scientist Eqifax, where he conducts research on machine learning and signal processing for the purposes of preventing fraud in the retail and financial sectors. He was previously with Pindrop. His research interests revolve around the interplay of control theory, signal processing, and machine learning for spatiotemporal data. He received his PhD in Electrical and Computer Engineering from the Georgia Institute of Technology in 2014  
15 and did a postdoc at Oklahoma State University with Chowdhary's group.

20 **Joshua Whitman** is a PhD candidate at the University of Illinois in Urbana-Champaign. He received Bachelors of Science degrees in Mechanical Engineering and Mathematics from Oklahoma State University in 2015, and his Masters of Science in Mechanical Engineering from the University of Illinois in 2018. His research is centered in the fields of machine learning, controls, and autonomy, and his work focuses on developing new methods for learning, monitoring, and controlling the dynamics of complex spatiotemporally-evolving systems.

25 **Girish Chowdhary** is an assistant professor at the University of Illinois at Urbana-Champaign and affiliated with Electrical and Computer Engineering, Agricultural and Biological Engineering, Computer Science, Aerospace Engineering, and is a member of the UIUC Coordinated Science Laboratory (CSL). He is the director of the Distributed Autonomous Systems laboratory and the Field Robotics Engineering and Science Hub (FRESH) at UIUC. He holds a PhD (2010) from Georgia Institute of Technology in Aerospace Engineering. He was a postdoc at the Laboratory for Information and Decision Systems (LIDS) of the Massachusetts Institute of Technology for about two years (2011-2013). He was an assistant professor at Oklahoma State University's  
30 Mechanical and Aerospace Engineering department (2013-2016). Prior to joining Georgia Tech, he also worked with the German Aerospace Center's (DLR's) Institute of Flight Systems for around three years (2003-2006). His undergraduate institution was the Royal Melbourne Institute of Technology in Australia. Girish's ongoing research interest is in theoretical insights and practical algorithms for adaptive autonomy with applications in field robotics.